Cell Reports

Article

Astroglial ER-mitochondria calcium transfer mediates endocannabinoid-dependent synaptic integration

Graphical abstract

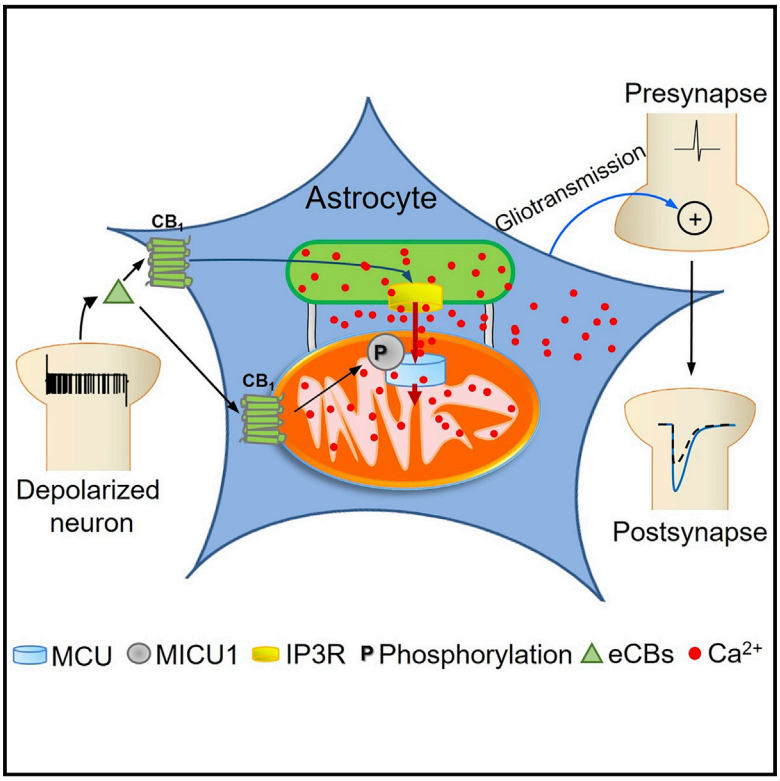

Authors

Roman Serrat, Ana Covelo, Vladimir Kouskoff, ..., Anna Beyeler, Sandrine Pouvreau, Giovanni Marsicano

Correspondence

sandrine.pouvreau@u-bordeaux.fr (S.P.), giovanni.marsicano@inserm.fr (G.M.)

In brief

Serrat et al. demonstrate that mitochondria-associated CB_1 ($mtCB_1$) receptors determine endocannabinoid-dependent intracellular calcium signaling in astrocytes to promote synaptic integration. Upon endocannabinoid mobilization, $mtCB_1$ receptors favor calcium transfer from ER to mitochondria through a specific molecular cascade involving the mitochondrial calcium uniporter, thereby shaping the dynamics of cytosolic calcium events.

Highlights

- ER/mitochondria contacts in astrocytes are determinants of synaptic integration
- Mitochondrial calcium uptake is actively modulated by $mtCB_1$
- Mitochondria-dependent calcium dynamics in astrocytes determine synaptic activity
- Astroglial $mtCB_1$ receptors are required for lateral synaptic plasticity

Serrat et al., 2021, Cell Reports 37, 110133
December 21, 2021 © 2021
https://doi.org/10.1016/j.celrep.2021.110133

CellPress

Cell Reports

CellPress
OPEN ACCESS

Article

Astroglial ER-mitochondria calcium transfer mediates endocannabinoid-dependent synaptic integration

Roman Serrat,[1,2,3] Ana Covelo,[1,2,9] Vladimir Kouskoff,[2,4,9] Sebastien Delcasso,[1,2,5,7,9] Andrea Ruiz-Calvo,[1,2] Nicolas Chenouard,[2,4] Carol Stella,[1,2] Corinne Blancard,[2,5] Benedicte Salin,[2,5] Francisca Julio-Kalajzić,[1,2] Astrid Cannich,[1,2] Federico Massa,[1,2] Marjorie Varilh,[1,2] Severine Deforges,[2,4] Laurie M. Robin,[1,2] Diego De Stefani,[6] Arnau Busquets-Garcia,[1,2,8] Frederic Gambino,[2,4] Anna Beyeler,[1,2] Sandrine Pouvreau,[1,2,4,10,*] and Giovanni Marsicano[1,2,10,11,*]

[1]Institut National de la Santé et de la Recherche Médicale (INSERM), U1215 NeuroCentre Magendie, 33077 Bordeaux, France
[2]University of Bordeaux, 33077 Bordeaux, France
[3]INRAE, Nutrition and Integrative Neurobiology, UMR 1286, Bordeaux, France
[4]Interdisciplinary Institute for Neuroscience, CNRS UMR 5297, 33000 Bordeaux, France
[5]Institut de Biochimie et Genetique Cellulaires, CNRS UMR 5095, Bordeaux, France
[6]Department of Biomedical Sciences, University of Padua, 35131 Padua, Italy
[7]Present address: Aquineuro, Bordeaux, France
[8]Present address: IMIM-Hospital del Mar Medical Research Institute, Barcelona, Spain
[9]These authors contributed equally
[10]Senior author
[11]Lead contact
*Correspondence: sandrine.pouvreau@u-bordeaux.fr (S.P.), giovanni.marsicano@inserm.fr (G.M.)
https://doi.org/10.1016/j.celrep.2021.110133

SUMMARY

Intracellular calcium signaling underlies the astroglial control of synaptic transmission and plasticity. Mitochondria-endoplasmic reticulum contacts (MERCs) are key determinants of calcium dynamics, but their functional impact on astroglial regulation of brain information processing is unexplored. We found that the activation of astrocyte mitochondrial-associated type-1 cannabinoid ($mtCB_1$) receptors determines MERC-dependent intracellular calcium signaling and synaptic integration. The stimulation of $mtCB_1$ receptors promotes calcium transfer from the endoplasmic reticulum to mitochondria through a specific molecular cascade, involving the mitochondrial calcium uniporter (MCU). Physiologically, $mtCB_1$-dependent mitochondrial calcium uptake determines the dynamics of cytosolic calcium events in astrocytes upon endocannabinoid mobilization. Accordingly, electrophysiological recordings in hippocampal slices showed that conditional genetic exclusion of $mtCB_1$ receptors or dominant-negative MCU expression in astrocytes blocks lateral synaptic potentiation, through which astrocytes integrate the activity of distant synapses. Altogether, these data reveal an endocannabinoid link between astroglial MERCs and the regulation of brain network functions.

INTRODUCTION

Astrocytes represent a large proportion of brain cells and exert key metabolic, structural, synaptic, and protective functions (Allaman et al., 2011; Haydon and Carmignoto, 2006; Perea et al., 2009; Pérez-Alvarez and Araque, 2013). In particular, accumulating evidence supports bidirectional communication between neurons and astrocytes at the so-called tripartite synapse, formed by pre- and post-synaptic elements surrounded by astroglial processes, thereby modulating information processing and behavior (Haydon and Carmignoto, 2006; Perea et al., 2009; Pérez-Alvarez and Araque, 2013).

Little is known about the intracellular astroglial mechanisms required to exert these functions, but it is clear that calcium dynamics at different subcellular astroglial microdomains are key functional elements of the tripartite synapse (Perea and Araque, 2005; Scemes and Giaume, 2006; Volterra et al., 2014). Astroglial calcium handling is a highly sophisticated process that is bidirectionally linked to synaptic activity and in which intracellular organelles such as endoplasmic reticulum (ER) and mitochondria play key active roles (Agarwal et al., 2017; Rizzuto et al., 2012; Simpson et al., 1997; Stephen et al., 2015). For instance, astroglial microdomain signaling has been suggested to involve calcium efflux from mitochondria (Agarwal et al., 2017). Moreover, data indicate that the positioning of mitochondria within astrocytic processes and their specific calcium-handling properties participate in the regulation of synaptic plasticity (Stephen et al., 2015). Mitochondria-endoplasmic reticulum contacts (MERCs) are key players of calcium signaling in many cells (Rizzuto et al., 1993) and have been recently described in astrocytes

This is an open access article under the CC BY-NC-ND license (http://creativecommons.org/licenses/by-nc-nd/4.0/).

(Göbel et al., 2020). However, their functional involvement in astrocyte calcium signaling and synaptic integration is unknown.

One of the most interesting functions of the tripartite synapse is lateral synaptic potentiation (LSP), through which astrocytes, upon neuronal depolarization, are able to enhance synaptic efficacy several tens of micrometers from the stimulation site (Gómez-Gonzalo et al., 2015; Navarrete and Araque, 2010), thereby contributing to fine-tuned synaptic and circuit integration (Covelo and Araque, 2016). LSP requires astroglial intracellular calcium elevations, which critically depend on the endogenous activation of type-1 cannabinoid (CB_1) receptors (Covelo and Araque, 2016; Navarrete and Araque, 2010). Discovered as the main target of synthetic and plant-derived cannabinoid drugs, these G protein-coupled receptors form, together with their endogenous ligands, the so-called endocannabinoid system (ECS), which is a key physiological determinant of synaptic and behavioral functions (Busquets-Garcia et al., 2018; Piomelli, 2003; Zou and Kumar, 2018).

Evidence indicates that besides their canonical localization at plasma membranes, functional intracellular CB_1 receptors can be observed in close association with mitochondria ($mtCB_1$ receptors; Bénard et al., 2012; Hebert-Chatelain et al., 2016; Jimenez-Blasco et al., 2020). The activation of $mtCB_1$ receptors decreases metabolic processes in brain cells, negatively affecting memory performance (Hebert-Chatelain et al., 2016), social interactions (Jimenez-Blasco et al., 2020), and likely regulating feeding behavior and neuroprotection (Hebert-Chatelain et al., 2016; Koch et al., 2015; Ma et al., 2015; Xu et al., 2016). In particular, anatomical data showed that astrocytes are endowed with a significant proportion of $mtCB_1$ receptors that are localized close to synapses (Gutiérrez-Rodríguez et al., 2018; Jimenez-Blasco et al., 2020). ER-dependent calcium signaling has been proposed as a mechanism through which astroglial CB_1 receptors trigger different functions of the tripartite synapse (Han et al., 2012; Oliveira da Cruz et al., 2016), including LSP (Navarrete and Araque, 2010). However, the precise astroglial intracellular mechanisms underlying these processes, the potential functional involvement of MERCs, and the particular implication of $mtCB_1$ receptors are unknown.

Here we asked whether astroglial MERC-dependent calcium signaling is regulated by the activation of $mtCB_1$ receptors and contributes to ECS-dependent synaptic plasticity. The results indicate that stimulation of CB_1 receptors promotes mitochondrial calcium accumulation in cultured astrocytes and in living animals. In particular, ER-dependent calcium entry into mitochondria is actively promoted by $mtCB_1$ receptors and regulates cytosolic calcium dynamics. This phenomenon plays a key role in LSP, thereby revealing an unforeseen link among mitochondrial functions, astroglial activity, and information processing in the brain.

RESULTS

Cannabinoid agonists induce mitochondrial calcium increase in astrocytes via $mtCB_1$ receptors

Previous reports have shown that CB_1 receptor activation causes changes in intracellular calcium levels in astrocytes (Hegyi et al., 2018; Navarrete and Araque, 2008, 2010). Thus, we asked whether $mtCB_1$ receptors participate in the regulation of astroglial calcium dynamics. To address this issue, we first used *CB_1*-knockout (KO) cultured astrocytes transfected with either the full-length CB_1 or the mutant DN22-CB_1, which lacks the first 22 amino acids of the receptor (Hebert-Chatelain et al., 2016; Jimenez-Blasco et al., 2020). This mutation strongly reduces the amount of $mtCB_1$ receptors in the cells and abolishes the mitochondrial effects of cannabinoid agonists, without altering non-mitochondrial CB_1 receptor-dependent actions (Hebert-Chatelain et al., 2016; Jimenez-Blasco et al., 2020). A semiquantitative analysis of confocal images of immunofluorescence staining of the transfected proteins revealed that this approach provides reliable and quantitatively similar expression of either CB_1 or DN22-CB_1 in cultured astrocytes (Figures S1A and S1B). We then used super-resolution STED microscopy to analyze both the overlap and the minimal distance between the mitochondrial marker Tom20 (mitochondrial outer membrane translocase 20 kDa) and the CB_1 or DN22-CB_1 proteins, respectively. The analysis of these STED images revealed that a relatively high proportion of CB_1 protein either overlapped (Figures S1A and S1C) or was placed a short distance from Tom20 (Figures S1D and S1E). Conversely, the overlap of DN22-CB_1 with Tom20 was strongly reduced compared with CB_1 (Figures S1A and S1C), and the distance from the mitochondrial marker was significantly higher (Figures S1D and S1E). Thus, the wild-type (WT) CB_1 protein significantly associates with astroglial mitochondria, whereas the DN22-CB_1 mutant displays lower mitochondrial association.

To simultaneously record mitochondrial and cytosolic calcium signals, we generated a mitochondrial genetically encoded indicator (Mito-GCaMP6s) and used it in combination with the cytosolic indicator RCaMP2 (Inoue et al., 2015). These constructs were co-transfected into *CB_1*-KO astrocytes, together with CB_1 or DN22-CB_1. The high-affinity cannabinoid agonist WIN 55,212-2 (WIN; 100 nM) increased cytosolic calcium levels in astrocytes expressing the CB_1 receptor, but not in control (Ctrl) *CB_1*-KO cells (Figures 1A–1C). This CB_1 receptor-dependent response was similar in DN22-CB_1 transfected astrocytes (Figures 1B–1D), indicating that the deletion of the first 22 amino acids does not impair the ability of CB_1 receptors to increase cytosolic calcium levels and that mitochondrial localization of the protein is unlikely to participate in this effect.

Interestingly, the same treatment induced an increase in mitochondrial calcium levels in astrocytes transfected with wild-type CB_1, but not in *CB_1*-KO cells (Figures 1A, 1E, and 1F). However, mitochondria from astrocytes expressing the DN22-CB_1 mutant did not respond to the WIN challenge (Figures 1D–1F). To rule out possible unspecific effects of our manipulations on the general ability of mitochondria to uptake calcium, the same cells used to study WIN effects were subsequently treated with the well-known astroglial and mitochondrial activator ATP (50 μM; Bowser and Khakh, 2007). Contrary to WIN, ATP caused a similar mitochondrial calcium response in all three conditions (Figure S1F).

Altogether, these data indicate that $mtCB_1$ receptors are dispensable for cannabinoid-induced increase of cytosolic calcium in astrocytes but are necessary for the cannabinoid-induced rise of the ion levels in astroglial mitochondria.

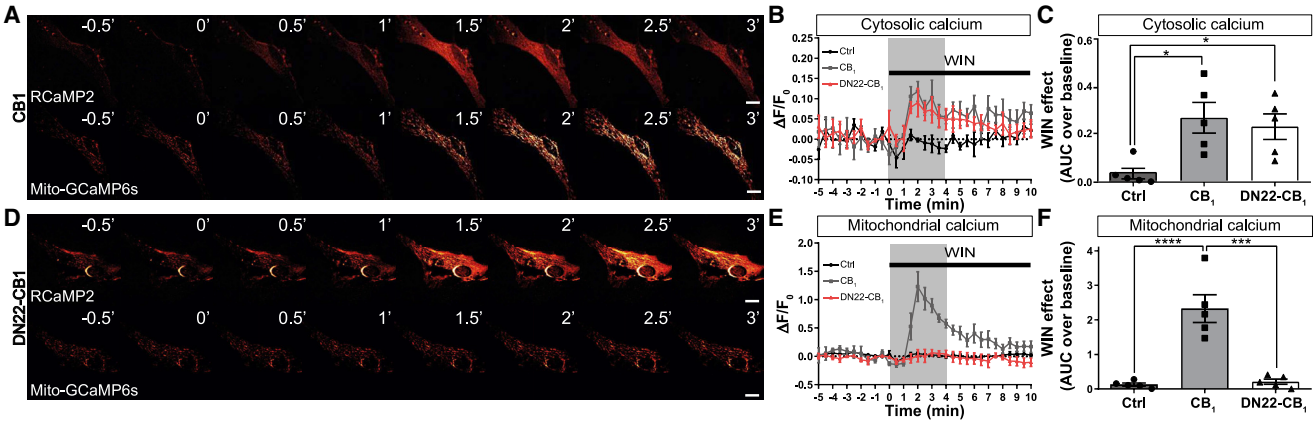

Figure 1. mtCB$_1$ activation increases mitochondrial calcium

(A and D) Representative time point RCaMP2 (upper panels) and Mito-GCaMP6s (bottom panels) images from CB$_1$ (A) or DN22-CB$_1$ (D) transfected astrocytes. WIN (100 nM) treatment was applied at time 0. Scale bar: 10 μm.

(B and E) $\Delta F/F_0$ traces from RCaMP2 (B) and Mito-GCaMP6s (E) images. Square gray panels show the quantified periods (4 min) in (C) and (F).

(C and F) WIN effect on calcium (area under the curve [AUC]) from $\Delta F/F_0$ traces in (B) and (E), respectively (n = 5 from 3 cultures).

Baseline: 1 min before WIN treatment. Data are represented as mean ± SEM. *p < 0.05, ***p < 0.001, ****p < 0.0001. See also Figure S1.

Molecular mechanisms of the mtCB$_1$ receptor-dependent mitochondrial calcium increase in astrocytes

Through the activation of inositol triphosphate receptor (IP3R), ER represents the major source of calcium in astrocytes (Sakuragi et al., 2017; Sherwood et al., 2017). Mitochondria physically contact ER at the level of MERCs (Csordás et al., 2018), allowing the transfer of calcium between these two organelles (Figure 2A). MERCs were also present in our *CB$_1$*-KO astrocyte cultures, and their structure was not altered by the expression of CB$_1$ or DN22-CB$_1$ receptors (Figure 2B; Figures S2A–S2D). To investigate the role of ER and MERCs in mtCB$_1$ receptor-dependent mitochondrial calcium increase, we first treated CB$_1$-expressing astrocytes with the blocker of the sarco/endoplasmic reticulum calcium-ATPase (SERCA) pump thapsigargin (TG; 1 μM), which empties ER from calcium (Figure 2A). TG treatment fully occluded the calcium responses to WIN in either the cytosol (Figure 2C; Figure S2E) or the mitochondria (Figure 2D; Figure S2F). Thus, ER mediates both cytosolic and mitochondrial cannabinoid-induced calcium increases.

IP3Rs are the main players of metabotropic control of cytosolic calcium in astrocytes and, interestingly, are present at MERCs (Bartok et al., 2019; Sakuragi et al., 2017; Sherwood et al., 2017). To determine whether IP3Rs are involved in the cannabinoid-mediated increase in cytosolic and/or mitochondrial calcium, we applied the IP3R antagonist 2-aminoethoxydiphenyl borate (2APB, 100 μM; Figure 2A) to CB$_1$-expressing astrocytes. 2APB drastically reduced CB$_1$ receptor-dependent cytosolic and mitochondrial calcium responses (Figures 2C and 2D; Figures S2E and S2F), indicating that both effects require the release of calcium from ER through IP3R.

The main channel for the entry of calcium into the mitochondrial matrix is the mitochondrial calcium uniporter (MCU; Rizzuto et al., 2012; Figure 2A). The application of MCU-inhibitor 11 (MCU-i11, 10 μM; Di Marco et al., 2020) to CB$_1$-expressing astrocytes did not alter the amplitude of the increase in bulk cytosolic calcium induced by WIN (Figure 2C; Figure S2E). However, this treatment strongly reduced WIN-induced increase in mitochondrial calcium levels (Figure 2D; Figure S2F), indicating that MCU activity is specifically involved in this mtCB$_1$ receptor-dependent effect.

Previous studies have shown that mtCB$_1$ receptors regulate mitochondrial oxygen consumption via the modulation of soluble adenylyl cyclase (sAC) in both neurons and astrocytes (Hebert-Chatelain et al., 2016; Jimenez-Blasco et al., 2020; Soria-Gomez et al., 2021). Surprisingly, sAC inhibitor KH7 (5 μM) was not able to affect cytosolic (Figure S2G) or mitochondrial (Figure S2H) calcium responses to WIN, indicating that this pathway is not involved in cannabinoid effects on calcium levels.

mtCB$_1$ receptors have been proposed to activate protein kinase B/AKT (hereafter called AKT; Xu et al., 2016). Recent data indicate that AKT stimulation increases the entrance of calcium in the mitochondrial matrix by phosphorylating mitochondrial calcium uptake protein 1 (MICU1), an important MCU modulator (Marchi et al., 2019). Immunocytochemistry approaches revealed that WIN treatment of CB$_1$-expressing astrocytes caused a fast and transient increase in AKT phosphorylation levels (p-AKT; Figures 2E and 2F), indicating that activation of CB$_1$ receptors triggers the AKT pathway in cultured astrocytes. The application of the AKT blocker MK-2206 (10 μM) did not impair CB$_1$ receptor-dependent cytosolic calcium increase (Figure 2G; Figure S2I), but it reduced the WIN effect on mitochondria (Figure 2H; Figure S2J). To further investigate the potential involvement of MCU and AKT/MICU1 signaling, a genetic strategy was designed. Astrocytes were co-transfected with a dominant-negative mutant version of MCU (dnMCU; Raffaello et al., 2013) or the non-phosphorylatable form MICU1-S124A (Marchi et al., 2019). The expression of either dnMCU or MICU1-S124A effectively blunted the WIN effect on mitochondrial calcium levels (Figure 2I; Figure S2K).

Altogether, these data indicate that the activation of IP3R through non-mitochondrial CB$_1$ receptors is sufficient for cannabinoid-induced cytosolic calcium increase in astrocytes.

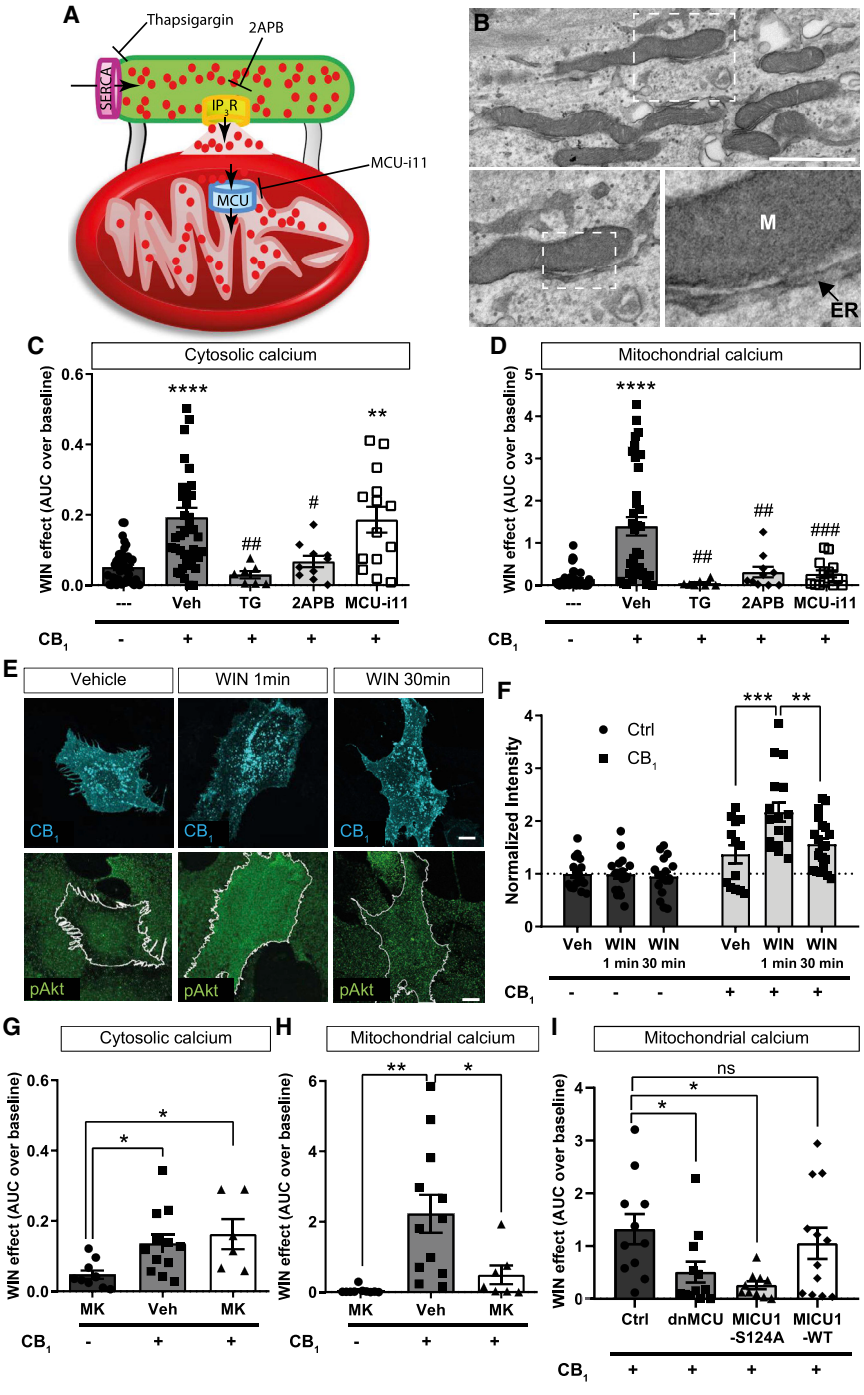

Figure 2. ER/IP3R/MCU and AKT pathways are necessary for CB_1-dependent mitochondrial calcium increase

(A) Schematic of the proteins involved in endoplasmic reticulum (ER; in green)-mitochondria (in red) calcium transfer and of the different drugs used to inhibit them.

(B) Representative electron microscopy image from *CB_1*-KO astrocytes. M, mitochondria. Scale bar: 0.5 μm.

(C and D) WIN effect on cytosolic (D) and mitochondrial (D) calcium levels (AUC) in negative control (CB_1−), vehicle control (Veh), thapsigargin (TG), 2APB, and MCU inhibitor 11 (MCU-i11) conditions (n = 7–41 from 31 cultures). Baseline: 1 min before WIN treatment. $\Delta F/F_0$ traces for (C) and (D) are shown in Figures S2E and S2F, respectively.

(E) Representative images from CB_1 transfected astrocytes in vehicle, WIN-1 min, and WIN-30 min conditions. Cyan, CB_1; green, p-AKT (T296). Scale bar: 10 μm.

(F) Normalized total intensity from cells shown in (E) in control (Ctrl) CB_1−, and CB_1+ transfected conditions (n = 13–20 from 4 cultures).

(G and H) WIN effect on cytosolic (G) and mitochondrial (H) calcium levels (AUC) in negative control CB_1−, Veh, and AKT-inhibitor (MK) conditions (n = 6–12 from 9 cultures). Baseline: 1 min before WIN treatment. $\Delta F/F_0$ traces for (G) and (H) are shown in Figures S2I and S2J, respectively.

(I) WIN effect on mitochondrial calcium (AUC) in CB_1+ transfected cells co-transfected with dnMCU, MICU1-S124A, or MICU1-WT (n = 10–12 from 7 cultures). Baseline: 1 min before WIN treatment. $\Delta F/F_0$ traces are shown in Figure S2K. Data are represented as mean ± SEM. *p < 0.05, **p < 0.01, ***p < 0.001, ****p < 0.0001; #p < 0.05, ##p < 0.01, ###p < 0.001 in comparison to the vehicle (CB_1+) condition. See also Figure S2.

Conversely, in addition to the stimulation of IP3R, mtCB_1 receptors, AKT signaling, MICU1 phosphorylation, and MCU activity are required for cannabinoid-induced mitochondrial calcium uptake.

CB_1 receptor activation increases mitochondrial calcium in astrocytes *in vivo*

Many differences exist between the cultured astrocytes and the same cells in living animals (Cahoy et al., 2008). To study whether CB_1 receptor-dependent mitochondrial calcium responses also occur *in vivo*, we generated an AAV virus expressing the sensor Mito-GCaMP6s under the promoter of the human glial fibrillary acidic protein (hGFAP; Hammond et al., 2017) to generate AAV-GFAP-Mito-GCAMP6s. The injection of this virus into the somatosensory cortex or the hippocampus resulted in specific expression of the calcium sensor in astrocytes (Figures 3A and 3B; Figure S3A). Four weeks after surgery, anesthetized, head-fixed wild-type and *CB_1*-KO mice carrying astroglial Mito-GCaMP6s expression in the somatosensory cortex were treated with the plant-derived cannabinoid Δ^9-tetrahydrocannabinol (THC, 10 mg/kg), and fluorescence levels were analyzed by two-photon microscopy (Figures 3C and 3D). Time course image analysis (Figure 3E) revealed that the THC treatment progressively increased the occurrence of mitochondrial calcium events in wild-type mice, but not in *CB_1*-KO mice (Figure 3F).

CellPress
OPEN ACCESS

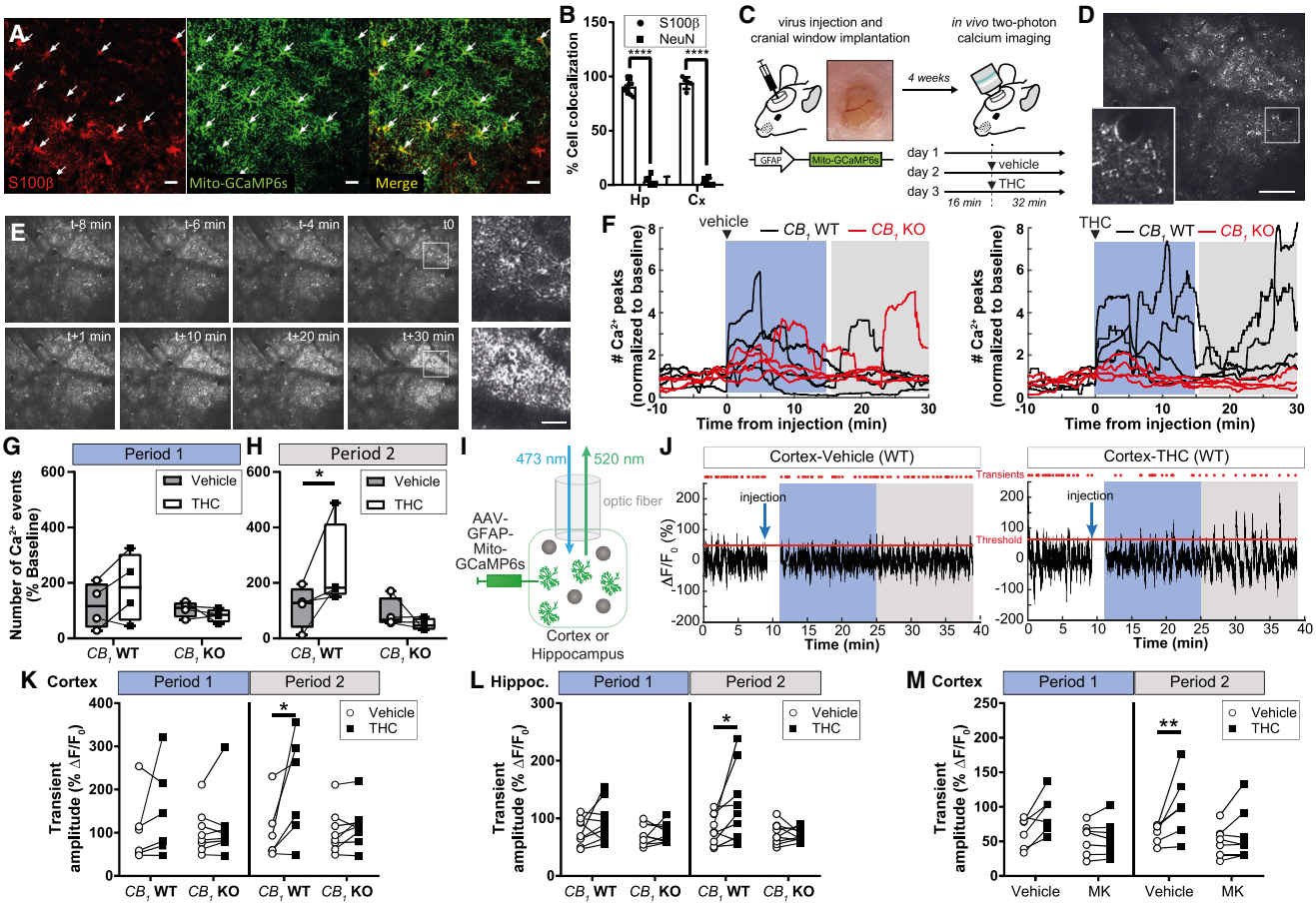

Figure 3. CB_1 activation induces mitochondrial calcium increase *in vivo*

(A) Representative images from mouse hippocampi injected with AAV-GFAP-Mito-GCaMP6s (in green) and stained with the astrocyte marker S100β (in red). Scale bar: 20 μm.

(B) Percentage of cell expressing Mito-GCaMP6s and stained with S100β (astrocytic marker) or NeuN (neuronal marker) in the hippocampi (Hp) and the cortex (Cx; n = 5–9 from 3 mice).

(C) Experimental two-photon imaging approach for *in vivo* recording of mitochondrial calcium dynamics in the mouse somatosensory cortex.

(D) Representative two-photon image. The squared image shows mitochondrial particles (yellow arrowheads). Scale bar: 100 μm.

(E) Representative time point two-photon images of the somatosensory cortex from a CB_1-WT mouse injected with AAV-GFAP-Mito-GCaMP6s. THC (10 mg/kg) treatment was applied at time 0. On the right, magnified images from time 0 and time 30 min (white squares). Scale bar: 30 μm.

(F) Normalized calcium traces from CB_1-WT and CB_1-KO mice injected with vehicle or THC. Blue and gray rectangles show the time window analyzed in (G) and (H).

(G and H) Average percentage of calcium events (normalized to day 1) between 0 to 15 min (G) or 15 to 30 min (H) in CB_1-WT and CB_1-KO mice treated with vehicle or THC (n = 4 mice).

(I) Scheme showing the fiber photometry imaging approach.

(J) Representative traces from the cortex of a CB_1-WT mouse injected with AAV-GFAP-Mito-GCaMP6s. Vehicle-injected (left panel) or THC-injected (10 mg/kg, right panel) mouse traces. Red dots correspond to detected transients above the threshold (median+2*MAD). Blue and gray rectangles show the time window of analyzed period 1 and period 2, respectively. The first minute before and after injection was removed to exclude mouse-handling/injection effects.

(K and L) Amplitude of the transients in the cortex (K) or the hippocampus (L) in CB_1-WT and CB_1-KO mice treated with vehicle or THC during the 2 periods highlighted in (J) (n = 6–9 mice).

(M) Amplitude of the transients in the cortex during the 2 periods highlighted in (J) in vehicle or MK-2206 (10 mg/kg) pretreated mice (n = 7 mice).

Data are represented as mean ± SEM. *p < 0.05, **p < 0.01, ****p < 0.0001. See also Figure S3.

In particular, whereas a non-significant trend effect of THC was already observed during the first 15 min post-injection, the increase in the number of calcium events became evident at min 15 to 30, with no changes in CB_1-KO mice (Figures 3G and 3H). These data indicate that THC increases astroglial mitochondrial calcium levels *in vivo*.

To investigate the effect of cannabinoid treatment in multiple brain regions simultaneously and in freely moving animals, we performed fiber photometry recordings in the hippocampus and somatosensory cortex of CB_1-KO mice or wild-type littermates carrying astroglial Mito-GCaMP6s expression (Figures 3A and 3B; Figure S3A). Basal calcium transients' amplitude, but not duration

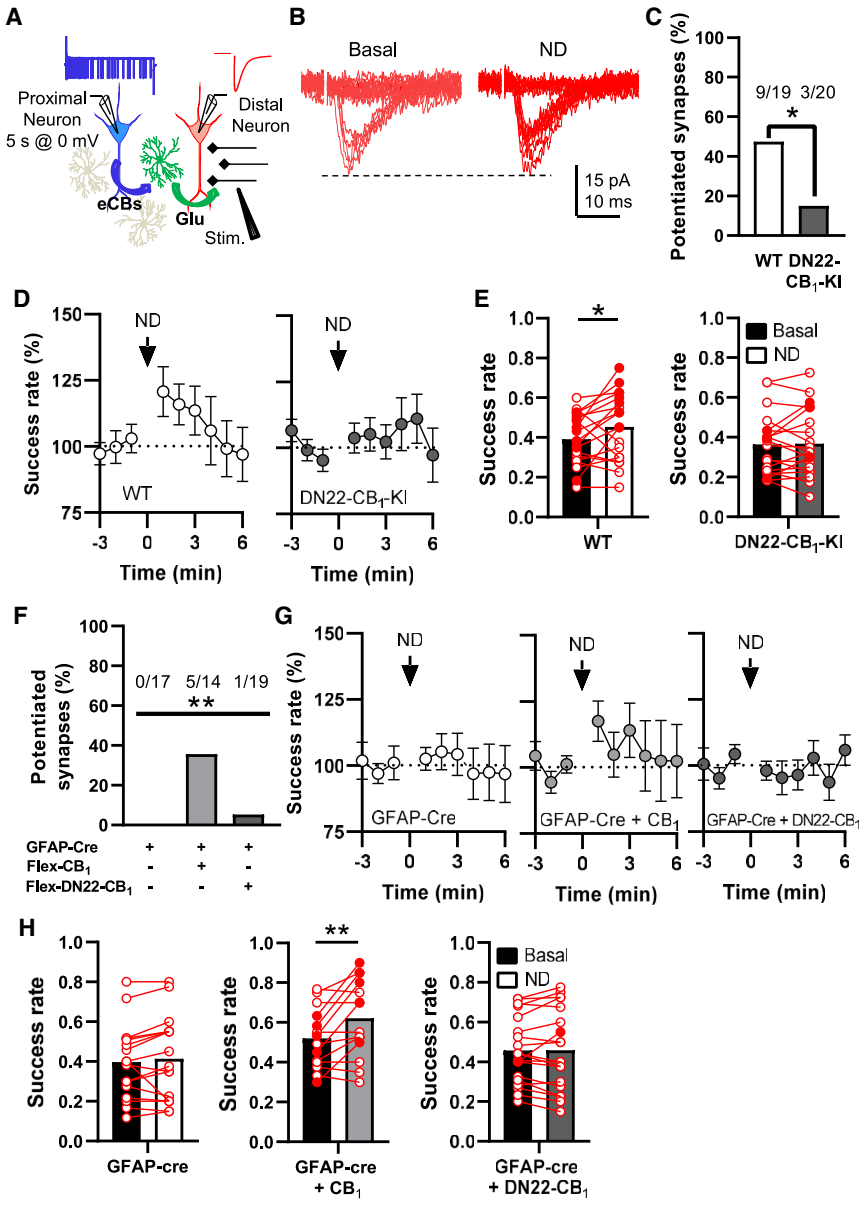

Figure 4. mtCB$_1$ is involved in lateral synaptic potentiation

(A) Scheme depicting the experimental approach. eCBs, endocannabinoids; Glu, glutamate.

(B) Representative traces obtained before (basal) and after neuronal depolarization (ND).

(C) Percentage of potentiated synapses recorded in WT and DN22-CB$_1$-KI hippocampal slices.

(D) Time course of the normalized success rate in WT and DN22-CB$_1$-KI conditions. The arrow indicates ND.

(E) Success rate before (basal) and after ND time in WT and DN22-CB$_1$-KI conditions. Red and white circles represent potentiated and non-potentiated synapses, respectively (n = 19–20 from 9 mice).

(F–H) Like (C)–(E), respectively, but from mice injected with viruses coding for GFAP-Cre, GFAP-Cre + CB$_1$, or GFAP-Cre + DN22-CB$_1$ (n = 14–19 from 10 mice).

Data are represented as mean ± SEM. *p < 0.05, **p < 0.01. See also Figure S4.

or frequency, was dramatically reduced in mice carrying the astroglial expression of dnMCU (Figures S3B and S3C), showing that the *in vivo* recorded events reflect calcium entrance into the mitochondria through MCU. The effects of vehicle or THC injections (10 mg/kg intraperitoneal [i.p.]; Figures 3I and 3J) on the amplitude, duration, and frequency of recorded calcium events were analyzed in 2 equal periods in the hippocampus and the somatosensory cortex simultaneously. No significant effects were observed during the first 15 min of recording (Figures 3K and 3L; Figures S3D–S3G). However, during the second half of recording, THC significantly increased the amplitudes of astroglial mitochondrial calcium signals in both the hippocampus and the cortex of *CB$_1$*-WT mice, but not of *CB$_1$*-KO littermates (Figures 3K and 3L). Despite some non-significant trends, the frequency and the duration of the transients were not altered by the drug (Figures S3D–S3G). To further investigate the potential involvement of the AKT signaling pathway, the AKT blocker MK-2206 (10 mg/kg i.p.) was administered before the THC injection. The drug did not affect cortical mitochondrial calcium events per se (Figure 3M; Figures S3H and S3I), but it prevented THC-dependent amplitude rise (Figure 3M; Figures S3H and S3I). Thus, systemic THC administration increases astroglial mitochondrial calcium levels in an AKT signaling-dependent way in the brain of freely moving animals.

Physiological role of mtCB$_1$ receptors in astrocyte-dependent synaptic integration

Neuronal depolarization induces the mobilization of endocannabinoids, leading to retrograde suppression of neurotransmitter release (Piomelli, 2003; Zou and Kumar, 2018). However, these endocannabinoids can also activate CB$_1$ receptors in neighboring astrocytes and, by increasing intracellular calcium activity, induce distal glutamate release and LSP (Covelo and Araque, 2016, 2018; Navarrete and Araque, 2008, 2010). To investigate the potential role of mtCB$_1$ receptors in this phenomenon, we performed simultaneous whole-cell electrophysiological recordings of two CA1 pyramidal neurons in acute hippocampal slices (>60 μm apart, termed proximal and distal neurons). Upon minimal stimulation of the Schaffer collaterals (Navarrete and Araque, 2010), the activity of putative single synapses onto the distal neuron was recorded. After neuronal depolarization (5 s at 0 mV) of the proximal neuron to induce endocannabinoid mobilization (Navarrete and Araque, 2010), we analyzed changes in synaptic parameters recorded in the distal neuron (Figure 4A). As expected (Navarrete and Araque, 2010), neuronal depolarization

induced an increase in the success rate in 9 of 19 distal neurons derived from wild-type animals (47.4%; Figures 4B–4E), without changes in the amplitude of evoked excitatory post-synaptic potentials (EPSCs; Figure 4B; Figure S4A), thereby indicating the occurrence of LSP. We then used a recently generated knockin (KI) mouse mutant line in which the DN22-CB_1 sequence replaces the wild-type CB_1 gene (DN22-CB_1-KI mice; Pagano Zottola et al., 2020; Soria-Gomez et al., 2021). These mutants lack the anatomical association of the CB_1 protein with mitochondria and do not display typical *in vivo* and *ex vivo* mitochondrial-related effects of cannabinoids (e.g., decrease of cellular respiration and amnesic effects; Pagano Zottola et al., 2020; Soria-Gomez et al., 2021). However, the mutant mice maintain other functions of CB_1 receptors, such as the pharmacological activation of G protein signaling or the physiological regulation of hippocampal inhibitory neurotransmission (Pagano Zottola et al., 2020; Soria-Gomez et al., 2021). Interestingly, basal synaptic parameters were not altered in hippocampal slices obtained from DN22-CB_1-KI mice (Figures S4B and S4C), whereas LSP was virtually absent (Figures 4C–4E; Figure S4A). These data show that $mtCB_1$ is required for LSP. However, because DN22-CB_1-KI mice carry the mutation in all body cells, these results do not provide information concerning the cellular location where $mtCB_1$ mediates LSP. To address this issue, we used a double viral strategy. CB_1-flox mice were locally injected in the hippocampus with AAV-hGFAP-Cre-IRES-mCherry to induce the deletion of the CB_1 gene from astrocytes (Figure S4D). Simultaneously, another AAV was injected, inducing Cre-dependent (FLEX system; Schnütgen et al., 2003) expression of the wild-type CB_1 or DN22-CB_1 receptor. LSP was absent from mice carrying a deletion of the *CB_1* gene in hippocampal astrocytes (Figures 4F–4H; Figures S4E–S4G). The re-expression of astroglial CB_1 receptors fully rescued LSP in these mice (Figures 4F–4H; Figures S4E–S4G). However, the re-expression of DN22-CB_1 was not sufficient to promote synaptic plasticity (Figures 4F–4H; Figures S4E–S4G), showing that astroglial $mtCB_1$ receptors are necessary for LSP.

Mitochondrial calcium uptake in astrocytes is essential for $mtCB_1$ receptor-dependent lateral synaptic potentiation

The results obtained so far indicate that $mtCB_1$ receptors are necessary for endocannabinoid-dependent LSP in the hippocampus and for CB_1 agonist-induced MCU-dependent increase of mitochondrial calcium in astrocytes. Thus, we asked whether mitochondrial calcium regulation might participate in the astroglial signaling underlying LSP (Navarrete and Araque, 2010). Cytosolic calcium dynamics were recorded in hippocampal slices expressing the GCaMP6f indicator in astrocytes, under resting conditions, and following LSP-inducing neuronal depolarization (Figure 5A; Figures S5A and S5B). Neuronal depolarization effectively induced an increase in the amplitude, frequency, spread, and duration of large astroglial calcium events (>40 μm^2 of the spreading coefficient; see STAR Methods; Figures 5B–5E) without affecting smaller ones (Figures S5C–S5F). Interestingly, whereas the application of MCU-i11 did not affect the depolarization-induced increase of astroglial calcium transient amplitude (Figure 5B; Figure S5B), it abolished the effects on the frequency, the spread, and the duration of these events (Figures 5C–5E). These data indicate that mitochondrial calcium handling specifically affects the dynamic changes of astroglial calcium signals accompanying neuronal-depolarization-induced LSP, which are known to be triggered by endocannabinoid mobilization (Gómez-Gonzalo et al., 2015; Hegyi et al., 2018; Martin-Fernandez et al., 2017; Min and Nevian, 2012; Navarrete and Araque, 2008, 2010; Navarrete et al., 2014; Oliveira da Cruz et al., 2016; Perez-Alvarez et al., 2014; Robin et al., 2018).

To further investigate whether this function of mitochondria participates in $mtCB_1$ receptor-dependent LSP, we directly addressed the role of MCU in this phenomenon. MCU-i11 strongly reduced the number of neurons undergoing depolarization-induced LSP (Figure 5F), abolishing the increase in success rate in distal synapses (Figures 5G and 5H), without altering the amplitude of EPSCs (Figure S5G). These results suggest that MCU activity is required for LSP in the hippocampus. However, control experiments revealed that MCU-i11 did not alter the amplitude of basal EPSCs (Figure S5H) but did slightly increased the basal success rate (Figure S5I), suggesting that the blockade of LSP might be confounded by an occlusion effect of the drug. Moreover, MCU is expressed in both astrocytes and neurons (Márkus et al., 2016), leaving the possibility that its blockade impairs LSP through mechanisms other than a direct $mtCB_1$ receptor-dependent regulation of astroglial mitochondrial calcium. To control for these potential confounders, we adopted a genetic approach and generated an AAV carrying the expression of dnMCU in astrocytes *in vivo* (AAV-GFAP-dnMCU; Figure S5J). The expression of dnMCU in hippocampal astrocytes did not alter the basal EPSC amplitude or the success rate (Figures S5H and S5I). However, the astroglial expression of dnMCU blocked LSP (Figures 5F, 5I, and 5J; Figure S5G), thereby confirming the involvement of astrocytic MCU.

Altogether, these data show that mitochondrial calcium uptake by MCU controls both endocannabinoid-dependent cytosolic calcium dynamics and $mtCB_1$-dependent LSP.

DISCUSSION

This study reveals an unforeseen mechanism linking mitochondrial and MERC calcium dynamics in astrocytes and synaptic integration in hippocampal circuits. In particular, activation of $mtCB_1$ receptors in astrocytes promotes ER- and IP3R-dependent mitochondrial calcium entry, requiring AKT signaling, MICU1 phosphorylation, and MCU activity. Moreover, endogenous physiological activation of $mtCB_1$ receptors by neuronal depolarization regulates astroglial cellular calcium dynamics and thereby mediates lateral potentiation of excitatory synaptic transmission. Therefore, $mtCB_1$ receptor regulation of MERC functions is an important element of astroglial control of synaptic integration.

Besides other roles, mitochondria are known to uptake calcium, contributing to the shaping of cytosolic calcium dynamics and thereby to the regulation of several important cellular processes (Celsi et al., 2009; Duchen, 2000; O-Uchi et al., 2012; Santo-Domingo and Demaurex, 2010). Mitochondrial calcium uptake is generally considered a passive mechanism controlled by cytosolic calcium levels (Carafoli, 2003), although recent

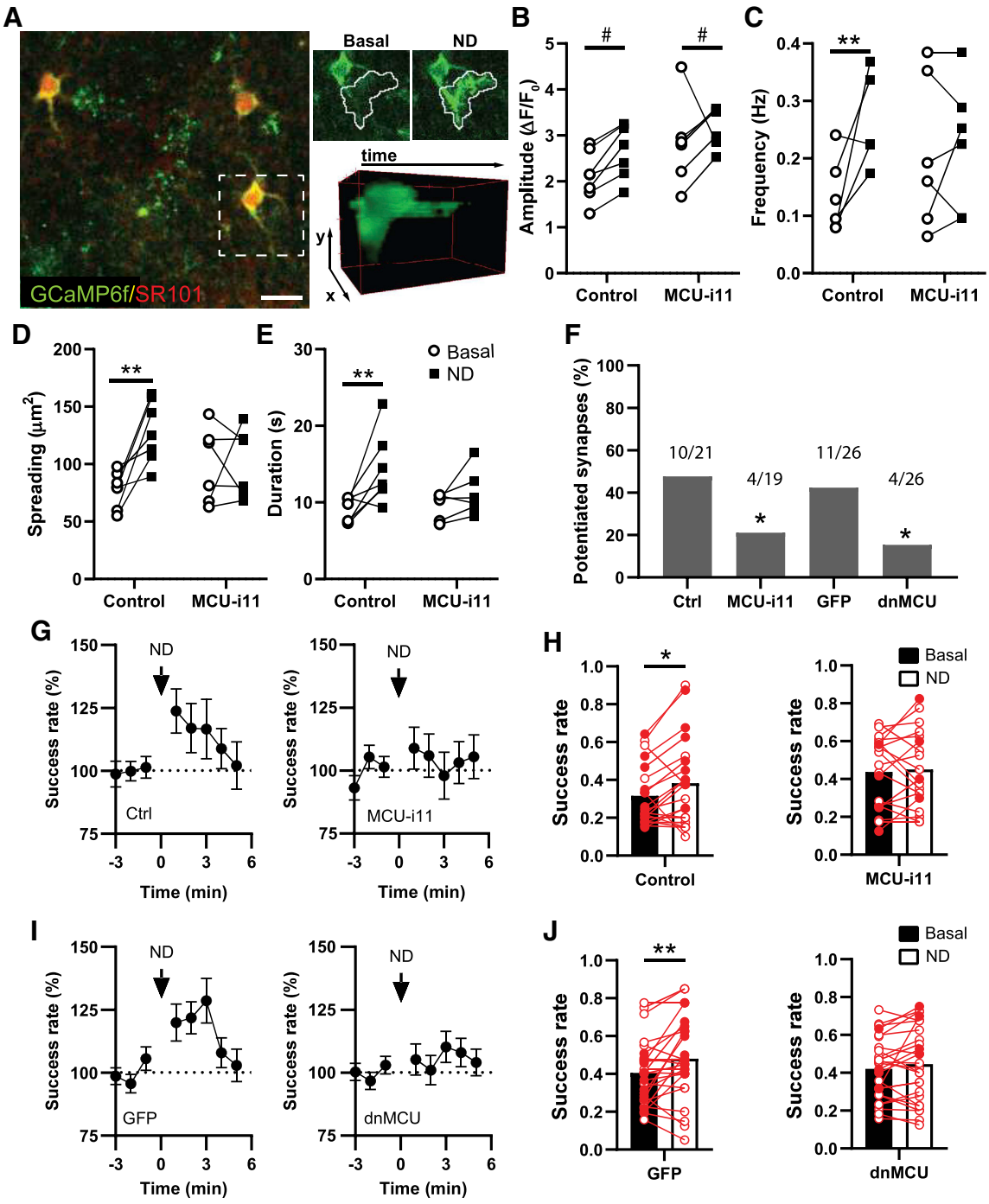

Figure 5. MCU blockade disturbs astrocyte-neuron signaling

(A) Left panel: representative confocal image from mouse hippocampi injected with AAV-GFAP-GCaMP6f (in green). Astrocyte marker SR101 is in red. Scale bar: 20 μm. Right panels: localization (white line) of a calcium event before or after ND and 3D reconstruction of the event in x, y, and t (see STAR Methods).

(B–E) Graphs obtained from calcium confocal imaging in hippocampal slices (A), showing (B) mean amplitude, (C) frequency, (D) mean spreading coefficient, and (E) mean duration of large calcium events (>40 μm^2) before (control) or 20 min after MCU-i11 treatment (n = 6–7 from 4 mice).

(F) Percentage of potentiated synapses recorded in different experimental conditions.

(G) Time course of the normalized probability of release in Ctrl and MCU-i11 conditions. The arrow indicates ND.

(H) Success rate before (basal) and after ND time in the Ctrl and MCU-i11 conditions shown in (G). Red and white circles represent potentiated and non-potentiated synapses, respectively (n = 19–21 from 15 mice).

(I and J) Like (G) and (H), but from mouse hippocampal slices injected with GFP or with dnMCU (n = 26 from 19 mice).

Data are represented as mean ± SEM. *p < 0.05, **p < 0.01; #p < 0.05 general stimulation effect on amplitude. See also Figure S5.

evidence suggests that this process might be actively regulated (Jhun et al., 2016; Marchi et al., 2019; Tarasova et al., 2019). Our data clearly show that $mtCB_1$ receptors actively promote mitochondrial calcium intake in astrocytes, independent of cytosolic calcium levels. Besides CB_1, other metabotropic receptors have been proposed to act on mitochondria calcium signaling (Abadir et al., 2011; Belous et al., 2006; Lahuna and Jockers, 2018; Suofu et al., 2017). For instance, the stimulation of P2Y2 purinergic receptors in *in vitro* isolated mitochondria can increase mitochondrial calcium (Belous et al., 2006). Our data show that the effects of cannabinoids on astroglial mitochondrial calcium levels are present both in cultured cells and *in vivo*, demonstrating that this function of metabotropic receptors is relevant to living and behaving animals.

By showing that $mtCB_1$ receptors are necessary for cannabinoid-induced mitochondrial, but not cytosolic, calcium increases, our data reinforce the idea that specific signaling cascades actively modulate calcium dynamics in these organelles. In particular, distinct subcellular pools of CB_1 receptors differentially participate in the modulation of subcellular calcium dynamics. The observation that inhibition of AKT or the expression of a non-phosphorylatable form of MICU1 reduces mitochondrial, but not cytosolic, cannabinoid-mediated increases of calcium supports this idea. Altogether, these data reveal that $mtCB_1$ receptors represent active regulators of dynamic mitochondrial calcium uptake in astrocytes through a molecular cascade involving IP3R, AKT, MICU1, and MCU.

CB_1 receptor-dependent cytosolic calcium increase in astrocytes mainly relies on the release of calcium from ER (present results; Navarrete and Araque, 2008, 2010). Our data indicate that ER calcium release is also needed for $mtCB_1$ receptor-dependent mitochondrial calcium increase. In our electron microscopy (EM) analysis of cultured astrocytes, almost 100% of mitochondria are located less than 100 nm from ER, a distance that permits calcium exchanges between the 2 organelles and defines MERCs (Csordás et al., 2018). In addition, previous EM studies of hippocampal slices have revealed that (1) astroglial $mtCB_1$ receptors are near synapses (less than 1 μm away; Gutiérrez-Rodríguez et al., 2018) and (2) MERCs are present in the astrocytic processes (Göbel et al., 2020). Hence, our data support the notion that $mtCB_1$ receptors are placed in the ideal position to regulate MERC-dependent calcium transfer and thereby modulate astrocytic calcium signaling.

Amplification sites for calcium waves in astrocytes are characterized by the presence of both mitochondria and ER proteins involved in calcium signaling (e.g., calreticulin and IP3R; Simpson et al., 1997). This suggests that MERC calcium transfer could be needed for the propagation of cytosolic calcium events. Abolition of cannabinoid-induced mitochondrial calcium entry by blocking MCU, removing $mtCB_1$, or inhibiting AKT does not affect the amplitude of the CB_1-dependent simultaneous cytosolic calcium increase in cultured astrocytes. This could be due to technical reasons. For instance, the indicator used to detect cytosolic calcium RCaMP2 has a low dynamic range, which could prevent the detection of small changes in amplitude (Inoue et al., 2015). However, the use of the larger dynamic range indicator GCaMP6f to detect cytosolic calcium in hippocampal slices also failed to reveal any difference in the amplitude of endocannabinoid-induced cytosolic calcium events in similar conditions. Thus, the lack of effect of the blockade of mitochondrial calcium uptake on the amplitude of cytosolic calcium transient seems to reflect physiological mechanisms rather than technical limits of the experiments. Indeed, it has been shown that mitochondria might act as poor dynamic buffers of bulk cytosolic calcium under physiological conditions, especially when other strong extrusion systems, such as plasma membrane and ER calcium pumps, are available, whereas their activity still regulates cytosolic calcium levels in specific microdomains (Boyman et al., 2014; Williams et al., 2013). Unfortunately, calcium dynamics in microdomains cannot be thoroughly addressed using classical calcium imaging techniques. Hence, further studies on the astrocytic calcium machinery are needed to dissect the role of mitochondria in the regulation of the amplitude of astrocytic calcium transients under physiological conditions.

Contrasting with the lack of effect on the amplitude, MCU inhibition affects the spatial and temporal spreading of astroglial cytosolic calcium events after activation of endocannabinoid signaling by neuronal depolarization. This indicates that $mtCB_1$-dependent regulation of MERC functions plays a key physiological role in the regulation of the dynamic properties of astroglial calcium signaling. However, mitochondria have been proposed to modulate calcium wave propagation in the opposite way, with impairment of mitochondrial function increasing the spreading and duration of calcium signals (Boitier et al., 1999; Jackson and Robinson, 2015; Reyes and Parpura, 2008). These studies used strong pharmacological stimulation of ER calcium release, whereas our data are based on physiological endogenous stimulations. Thus, this apparent discrepancy could originate from differences in methodological approaches. However, it is also possible that the $mtCB_1$ receptor-dependent mitochondrial calcium increase exerts a specific signaling function. For instance, it might prevent negative feedback on IP3R following changes in local calcium concentrations, which has been proposed to regulate cytosolic calcium spreading (Foskett and Daniel Mak, 2010). Altogether, our results suggest that ER/mitochondria calcium transfer induced by activation of $mtCB_1$ receptors is important for the dynamic propagation of cytosolic calcium waves in astrocytes.

Over the course of the last 20 years, numerous studies have led to the conclusion that neuronal network functions result from the coordinated activity of astrocytes and neurons (Covelo and Araque, 2016). It is well known that astroglial intracellular calcium elevations induced by synaptic transmission are key elements of astrocyte/neuron interactions (Araque et al., 2001; Nedergaard et al., 2003; Perea and Araque, 2005; Volterra and Meldolesi, 2005). However, how astroglial calcium is regulated to provide specificity to these functions is still largely elusive (Semyanov, 2019; Volterra et al., 2014). In this context, the double location of CB_1 receptors at plasma and mitochondrial membranes might represent a way to provide signal specificity to calcium increases through a two-step action. First, the activation of plasma membrane CB_1 receptors might promote ER calcium release into the cytosol. Then, $mtCB_1$ receptor stimulation might locally determine the dynamics of calcium spreading required to provide signaling specificity to astrocyte/neuron interactions. Thus, these data pave the way to the idea that multiple control

mechanisms of intracellular calcium levels and dynamics are necessary for proper astroglial regulation of synaptic functions. Moreover, they underline that beyond ion absolute levels, the dynamics of calcium diffusion within the cytoplasm (in this case, controlled by mtCB$_1$ receptors) determine astrocyte synaptic regulation. One example of this phenomenon is the astroglial CB$_1$ receptor-induced LSP of excitatory synapses (Covelo and Araque, 2016; Navarrete and Araque, 2010). By allowing the coordinated activity of neurons that are not necessarily synaptically connected, LSP likely represents a mechanism to expand the computational impact of neuronal networks (Covelo and Araque, 2016). Our data show that the control of calcium dynamics by the activation of mtCB$_1$ receptors is required to express LSP. LSP has been described since its discovery as a phenomenon occurring in only part of the analyzed neuronal pairs (Navarrete and Araque, 2008, 2010). This is understandable if we consider that the choice of the proximal and distal neurons is necessarily blind, with the distance between them the only available parameter (Navarrete and Araque, 2008, 2010). However, the fact that two neurons are close to each other does not guarantee that they are connected by one or several interposed astrocytes. Thus, because of the large number of naturally occurring failures, the LSP effect might appear weak (approx. 20%) if, as done in this study, all experiments are considered. However, the amplitude of LSP in control experiments is higher (>50%) if only potentiated neurons are considered, indicating the likely physiological importance of the phenomenon. Therefore, astroglial mtCB$_1$ receptor-dependent control of MERCs functions actively participates in synaptic plasticity and likely contributes regulating complex information processing in the brain.

Overall, our findings unravel the importance of astroglial mitochondria and MERCs in shaping neuronal network activity and uncover a mechanism of action of CB$_1$ receptor signaling in the brain.

Limitations of the study

Technical limitations of the study

Two limitations regarding *in vivo* calcium imaging in astrocytes and expression of exogenous CB$_1$ should be mentioned. First, like most imaging approaches, the possibility to record mitochondrial calcium *in vivo* is based on viral-mediated protein expression, which is inevitably accompanied by a certain degree of gliosis (Ortinski et al., 2010). Therefore, we cannot exclude that our recordings also include reactive astrocytes. Nevertheless, our data state the principle that THC can increase mitochondrial calcium levels via CB$_1$ in astrocytes of living and freely moving animals.

Second, the *ex vivo* immunostaining of CB$_1$-*myc* or DN22-CB$_1$-*myc* Cre-dependent viral expression in the brains of *CB$_1$*-flox mice locally injected with AAV-GFAP-Cre and AAV-Flex-CB$_1$-*myc* or AAV-Flex-DN22-CB$_1$-*myc* (deletion and re-expression approach) could not be performed. These recombinant proteins are tagged with the *myc* epitope to be recognized by anti-*myc* antibodies, thereby allowing their distinction from endogenous CB$_1$ receptors. Unfortunately, at the moment of performing these experiments, the company BioLegend discontinued the production of the anti-*myc* antiserum polyclonal rabbit anti c-*myc* 906301, which has been our standard tool for this type of analysis (*ex vivo* determination of *myc*-tagged proteins). Despite several attempts with many other commercially available antisera from the same or other companies, we were not able to find anyone providing specific staining in positive controls. Therefore, it is unfortunately not possible to detect the Cre-dependent expression of CB$_1$ or DN22-CB$_1$ in the brain of virally injected mice at the moment. Nevertheless, Figure S6D clearly shows that Cre recombinase expression is highly restricted to astroglial cells. Therefore, although we cannot fully exclude undesired expression patterns, we are confident that the Cre-dependent viral expression of CB$_1$ and DN22-CB$_1$ in these experiments was also highly enriched in hippocampal astrocytes.

Conceptual limitations of the study

Two questions regarding lateral synaptic potentiation have not been addressed in this study, because we believe they are beyond its scope. First, we did not investigate how the proximal neuron causes an increase in the frequency of astrocyte calcium events during depolarization. There is abundant literature, using CB$_1$ antagonists and global or conditional astroglial *CB$_1$*-KO mice, clearly showing that an important mechanism of depolarization-induced astrocyte calcium rise is the neuronal release of endocannabinoids and the activation of astroglial CB$_1$ receptors (Andrade-Talavera et al., 2016; Gómez-Gonzalo et al., 2015; Hegyi et al., 2018; Kőszeghy et al., 2015; Kovács et al., 2017; Martin-Fernandez et al., 2017; Martín et al., 2015; Min and Nevian, 2012; Navarrete and Araque, 2008, 2010; Perez-Alvarez et al., 2014; Rasooli-Nejad et al., 2014; Robin et al., 2018). Because this is an accepted idea in the field (Metna-Laurent and Marsicano, 2015; Navarrete et al., 2014; Oliveira da Cruz et al., 2016), we originally assumed the neurotransmitter involved is endocannabinoid. This was confirmed by LSP being absent from the DN22-CB$_1$ mutant mice (Figures 4A–4E), providing additional clear evidence that specific CB$_1$ receptor subpopulations are required in the process. Moreover, deletion/rescue data clearly showed that calcium-dependent LSP requires mtCB$_1$ receptors in astrocytes (Figures 4F–4H). Hence, our data confirm the accepted idea that endocannabinoids derived from depolarized neurons and CB$_1$ receptor activation in neighboring astrocytes are necessary to induce calcium events eventually leading to astroglial control of synaptic plasticity.

Second, we did not investigate how the astrocyte affects the distal neuron following depolarization to cause LSP, because the nature of the potential gliotransmitters involved has been addressed in several previous studies (Covelo and Araque, 2018; Gómez-Gonzalo et al., 2015; Martín et al., 2015; Martin-Fernandez et al., 2017; Navarrete and Araque, 2008, 2010; Perez-Alvarez et al., 2014) and clearly falls beyond the aims of the present work. Our electrophysiological experiments aimed to identify possible functional implications of our discovery that mtCB$_1$ receptors control calcium dynamics in astrocytes.

STAR★METHODS

Detailed methods are provided in the online version of this paper and include the following:

- KEY RESOURCES TABLE

SUPPLEMENTAL INFORMATION

Supplemental information can be found online at https://doi.org/10.1016/j.celrep.2021.110133.

ACKNOWLEDGMENTS

This study is dedicated to the memory of our friend and colleague Federico Massa. Imaging studies were performed at the Bordeaux Imaging Center, a service unit of the CNRS-INSERM and Bordeaux University, member of the national infrastructure France BioImaging supported by the French National Research Agency (ANR-10-INBS-04). The help of Christel Poujol, Sébastien Marais, and Fabrice Cordelières is acknowledged. We also thank Delphine Gonzales, Nathalie Aubailly, and all personnel of the Animal Facilities of the NeuroCentre Magendie for mouse care. We thank the Biochemistry Platform of Bordeaux NeuroCampus for help. We also thank all members of Marsicano's lab for useful discussions and for their support. We thank Manuel Rojo for support in electron microscopy. We thank Haruhiko Bito for providing Rcamp2 plasmid. We thank Paolo Pinton for providing MICU1 plasmids. We thank Guillaume Ferreira for support and Jean-Luc Morel and Alfonso Araque for critically reading the manuscript. This work was funded by INSERM, the European Research Council (Endofood, ERC-2010-StG-260515; CannaPreg, ERC-2014-PoC-640923; and MiCaBra, ERC-2017-AdG-786467), the Fondation pour la Recherche Medicale (FRM; DRM20101220445), the Human Frontiers Science Program, Region Nouvelle Aquitaine, the Agence Nationale de la Recherche (ANR; NeuroNutriSens ANR-13-BSV4-0006 and ORUPS ANR-16-CE37-0010-01), BRAIN (ANR-10-LABX-0043) to G.M., Labex Brain (CANNACALC) to S.P. and F.M., and Eu-Fp7 (FP7-PEOPLE-2013-IEF-623638) and MINECO from AEI (RYC-2017-21776) to A.B.-G.

AUTHOR CONTRIBUTIONS

R.S. and C.S. performed and analyzed live cell-imaging recordings. A. Covelo performed and analyzed electrophysiological experiments. A.R.-C. performed and A.R.-C. and R.S. analyzed STED-microscopy experiments. C.B. and B.S. performed and R.S. analyzed electron microscopy experiments. V.K., N.C., and F.G. performed and analyzed two-photon recordings. R.S., S. Delcasso, A.B.-G., and A.B. performed and analyzed fiber photometry experiments. A. Covelo and S.P. performed and R.S. and S.P. analyzed cytosolic calcium experiments. F.J.-K. and M.V. performed immunohistochemistry experiments. A. Cannich contributed to experiments using viral vectors. S. Deforges contributed to plasmid cloning. R.S., A. Covelo, G.M., and S.P. wrote the manuscript. R.S., F.M., G.M., and S.P. conceived and supervised the whole project, and R.S., G.M., and S.P. supervised the writing of the manuscript. All authors edited and approved the manuscript. This study emerged from a conceptual combination effort between G.M. (CB_1 and $mtCB_1$ receptor signaling) and S.P. (MERCS and calcium signaling). The expertise of both authors was equally important for the design and the supervision of the project, justifying the presence of two senior authors.

DECLARATION OF INTERESTS

The authors declare no competing interests.

Received: July 16, 2020
Revised: October 8, 2021
Accepted: November 23, 2021
Published: December 21, 2021, corrected online September 27, 2022

REFERENCES

Abadir, P.M., Foster, D.B., Crow, M., Cooke, C.A., Rucker, J.J., Jain, A., Smith, B.J., Burks, T.N., Cohn, R.D., Fedarko, N.S., et al. (2011). Identification and characterization of a functional mitochondrial angiotensin system. Proc. Natl. Acad. Sci. USA *108*, 14849–14854.

Agarwal, A., Wu, P.H., Hughes, E.G., Fukaya, M., Tischfield, M.A., Langseth, A.J., Wirtz, D., and Bergles, D.E. (2017). Transient Opening of the Mitochondrial Permeability Transition Pore Induces Microdomain Calcium Transients in Astrocyte Processes. Neuron *93*, 587–605.e7.

Akerboom, J., Carreras Calderón, N., Tian, L., Wabnig, S., Prigge, M., Tolö, J., Gordus, A., Orger, M.B., Severi, K.E., Macklin, J.J., et al. (2013). Genetically encoded calcium indicators for multi-color neural activity imaging and combination with optogenetics. Front. Mol. Neurosci. *6*, 2.

Allaman, I., Bélanger, M., and Magistretti, P.J. (2011). Astrocyte-neuron metabolic relationships: for better and for worse. Trends Neurosci. *34*, 76–87.

Allen, C., and Stevens, C.F. (1994). An evaluation of causes for unreliability of synaptic transmission. Proc. Natl. Acad. Sci. USA *91*, 10380–10383.

Andrade-Talavera, Y., Duque-Feria, P., Paulsen, O., and Rodríguez-Moreno, A. (2016). Presynaptic Spike Timing-Dependent Long-Term Depression in the Mouse Hippocampus. Cereb Cortex *26*, 3637–3654.

Araque, A., Carmignoto, G., and Haydon, P.G. (2001). Dynamic signaling between astrocytes and neurons. Annu. Rev. Physiol. *63*, 795–813.

Bartok, A., Weaver, D., Golenár, T., Nichtova, Z., Katona, M., Bánsághi, S., Alzayady, K.J., Thomas, V.K., Ando, H., Mikoshiba, K., et al. (2019). IP_3 receptor isoforms differently regulate ER-mitochondrial contacts and local calcium transfer. Nat. Commun. *10*, 3726.

Belous, A.E., Jones, C.M., Wakata, A., Knox, C.D., Nicoud, I.B., Pierce, J., and Chari, R.S. (2006). Mitochondrial calcium transport is regulated by P2Y1- and P2Y2-like mitochondrial receptors. J. Cell. Biochem. *99*, 1165–1174.

Bénard, G., Massa, F., Puente, N., Lourenço, J., Bellocchio, L., Soria-Gómez, E., Matias, I., Delamarre, A., Metna-Laurent, M., Cannich, A., et al. (2012). Mitochondrial CB_1 receptors regulate neuronal energy metabolism. Nat. Neurosci. *15*, 558–564.

Boitier, E., Rea, R., and Duchen, M.R. (1999). Mitochondria exert a negative feedback on the propagation of intracellular Ca2+ waves in rat cortical astrocytes. J. Cell Biol. *145*, 795–808.

Bowser, D.N., and Khakh, B.S. (2007). Vesicular ATP is the predominant cause of intercellular calcium waves in astrocytes. J. Gen. Physiol. *129*, 485–491.

Boyman, L., Chikando, A.C., Williams, G.S., Khairallah, R.J., Kettlewell, S., Ward, C.W., Smith, G.L., Kao, J.P., and Lederer, W.J. (2014). Calcium movement in cardiac mitochondria. Biophys. J. *107*, 1289–1301.

Busquets-Garcia, A., Bains, J., and Marsicano, G. (2018). CB_1 Receptor Signaling in the Brain: Extracting Specificity from Ubiquity. Neuropsychopharmacology *43*, 4–20.

Cahoy, J.D., Emery, B., Kaushal, A., Foo, L.C., Zamanian, J.L., Christopherson, K.S., Xing, Y., Lubischer, J.L., Krieg, P.A., Krupenko, S.A., et al. (2008). A transcriptome database for astrocytes, neurons, and oligodendrocytes: a new resource for understanding brain development and function. J. Neurosci. *28*, 264–278.

Carafoli, E. (2003). Historical review: mitochondria and calcium: ups and downs of an unusual relationship. Trends Biochem. Sci. *28*, 175–181.

Celsi, F., Pizzo, P., Brini, M., Leo, S., Fotino, C., Pinton, P., and Rizzuto, R. (2009). Mitochondria, calcium and cell death: a deadly triad in neurodegeneration. Biochim. Biophys. Acta *1787*, 335–344.

Chevaleyre, V., and Castillo, P.E. (2004). Endocannabinoid-mediated metaplasticity in the hippocampus. Neuron *43*, 871–881.

Covelo, A., and Araque, A. (2016). Lateral regulation of synaptic transmission by astrocytes. Neuroscience *323*, 62–66.

Covelo, A., and Araque, A. (2018). Neuronal activity determines distinct gliotransmitter release from a single astrocyte. eLife *7*, e32237.

Csordás, G., Weaver, D., and Hajnóczky, G. (2018). Endoplasmic Reticulum-Mitochondrial Contactology: Structure and Signaling Functions. Trends Cell Biol. *28*, 523–540.

Di Marco, G., Vallese, F., Jourde, B., Bergsdorf, C., Sturlese, M., De Mario, A., Techer-Etienne, V., Haasen, D., Oberhauser, B., Schleeger, S., et al. (2020). A High-Throughput Screening Identifies MICU1 Targeting Compounds. Cell Rep. *30*, 2321–2331.e6.

Duchen, M.R. (2000). Mitochondria and Ca(2+)in cell physiology and pathophysiology. Cell Calcium *28*, 339–348.

Foskett, J.K., and Daniel Mak, D.O. (2010). Regulation of IP(3)R Channel Gating by Ca(2+) and Ca(2+) Binding Proteins. Curr. Top. Membr. *66*, 235–272.

Göbel, J., Engelhardt, E., Pelzer, P., Sakthivelu, V., Jahn, H.M., Jevtic, M., Folz-Donahue, K., Kukat, C., Schauss, A., Frese, C.K., et al. (2020). Mitochondria-Endoplasmic Reticulum Contacts in Reactive Astrocytes Promote Vascular Remodeling. Cell Metab. *31*, 791–808.e8.

Gambino, F., Pagès, S., Kehayas, V., Baptista, D., Tatti, R., Carleton, A., and Holtmaat, A. (2014). Sensory-evoked LTP driven by dendritic plateau potentials *in vivo*. Nature *515*, 116–119.

Gómez-Gonzalo, M., Navarrete, M., Perea, G., Covelo, A., Martín-Fernández, M., Shigemoto, R., Luján, R., and Araque, A. (2015). Endocannabinoids Induce Lateral Long-Term Potentiation of Transmitter Release by Stimulation of Gliotransmission. Cereb. Cortex *25*, 3699–3712.

Gutiérrez-Rodríguez, A., Bonilla-Del Río, I., Puente, N., Gómez-Urquijo, S.M., Fontaine, C.J., Egaña-Huguet, J., Elezgarai, I., Ruehle, S., Lutz, B., Robin, L.M., et al. (2018). Localization of the cannabinoid type-1 receptor in subcellular astrocyte compartments of mutant mouse hippocampus. Glia *66*, 1417–1431.

Hammond, S.L., Leek, A.N., Richman, E.H., and Tjalkens, R.B. (2017). Cellular selectivity of AAV serotypes for gene delivery in neurons and astrocytes by neonatal intracerebroventricular injection. PLoS ONE *12*, e0188830.

Han, J., Kesner, P., Metna-Laurent, M., Duan, T., Xu, L., Georges, F., Koehl, M., Abrous, D.N., Mendizabal-Zubiaga, J., Grandes, P., et al. (2012). Acute cannabinoids impair working memory through astroglial CB1 receptor modulation of hippocampal LTD. Cell *148*, 1039–1050.

Haydon, P.G., and Carmignoto, G. (2006). Astrocyte control of synaptic transmission and neurovascular coupling. Physiol. Rev. *86*, 1009–1031.

Hebert-Chatelain, E., Desprez, T., Serrat, R., Bellocchio, L., Soria-Gomez, E., Busquets-Garcia, A., Pagano Zottola, A.C., Delamarre, A., Cannich, A., Vincent, P., et al. (2016). A cannabinoid link between mitochondria and memory. Nature *539*, 555–559.

Hegyi, Z., Oláh, T., Kőszeghy, Á., Piscitelli, F., Holló, K., Pál, B., Csernoch, L., Di Marzo, V., and Antal, M. (2018). CB_1 receptor activation induces intracellular Ca^{2+} mobilization and 2-arachidonoylglycerol release in rodent spinal cord astrocytes. Sci. Rep. *8*, 10562.

Holtmaat, A., Bonhoeffer, T., Chow, D.K., Chuckowree, J., De Paola, V., Hofer, S.B., Hübener, M., Keck, T., Knott, G., Lee, W.C., et al. (2009). Long-term, high-resolution imaging in the mouse neocortex through a chronic cranial window. Nat. Protoc. *4*, 1128–1144.

Inoue, M., Takeuchi, A., Horigane, S., Ohkura, M., Gengyo-Ando, K., Fujii, H., Kamijo, S., Takemoto-Kimura, S., Kano, M., Nakai, J., et al. (2015). Rational design of a high-affinity, fast, red calcium indicator R-CaMP2. Nat. Methods *12*, 64–70.

Isaac, J.T., Hjelmstad, G.O., Nicoll, R.A., and Malenka, R.C. (1996). Long-term potentiation at single fiber inputs to hippocampal CA1 pyramidal cells. Proc. Natl. Acad. Sci. USA *93*, 8710–8715.

Jackson, J.G., and Robinson, M.B. (2015). Reciprocal Regulation of Mitochondrial Dynamics and Calcium Signaling in Astrocyte Processes. J. Neurosci. *35*, 15199–15213.

Jhun, B.S., Mishra, J., Monaco, S., Fu, D., Jiang, W., Sheu, S.S., and O-Uchi, J. (2016). The mitochondrial Ca2+ uniporter: regulation by auxiliary subunits and signal transduction pathways. Am. J. Physiol. Cell Physiol. *311*, C67–C80.

Jimenez-Blasco, D., Busquets-Garcia, A., Hebert-Chatelain, E., Serrat, R., Vicente-Gutierrez, C., Ioannidou, C., Gómez-Sotres, P., Lopez-Fabuel, I., Resch-Beusher, M., Resel, E., et al. (2020). Glucose metabolism links astroglial mitochondria to cannabinoid effects. Nature *583*, 603–608.

Koch, M., Varela, L., Kim, J.G., Kim, J.D., Hernández-Nuño, F., Simonds, S.E., Castorena, C.M., Vianna, C.R., Elmquist, J.K., Morozov, Y.M., et al. (2015). Hypothalamic POMC neurons promote cannabinoid-induced feeding. Nature *519*, 45–50.

Kőszeghy, Á., Kovács, A., Bíró, T., Szücs, P., Vincze, J., Hegyi, Z., Antal, M., and Pál, B. (2015). Endocannabinoid signaling modulates neurons of the pedunculopontine nucleus (PPN) via astrocytes. Brain Struct Funct *220*, 3023–3041.

Kovács, A., Bordás, C., Bíró, T., Hegyi, Z., Antal, M., Szücs, P., and Pál, B. (2017). Direct presynaptic and indirect astrocyte-mediated mechanisms both contribute to endocannabinoid signaling in the pedunculopontine nucleus of mice. Brain Struct Funct *222*, 247–266.

Kreitzer, A.C., and Regehr, W.G. (2001). Retrograde inhibition of presynaptic calcium influx by endogenous cannabinoids at excitatory synapses onto Purkinje cells. Neuron *29*, 717–727.

Lahuna, O., and Jockers, R. (2018). [Mitochondrial signaling of G protein-coupled receptors]. Biol. Aujourdhui *212*, 21–26.

Lütcke, H., Murayama, M., Hahn, T., Margolis, D.J., Astori, S., Zum Alten Borgloh, S.M., Göbel, W., Yang, Y., Tang, W., Kügler, S., et al. (2010). Optical recording of neuronal activity with a genetically-encoded calcium indicator in anesthetized and freely moving mice. Front. Neural Circuits *4*, 9.

Ma, L., Jia, J., Niu, W., Jiang, T., Zhai, Q., Yang, L., Bai, F., Wang, Q., and Xiong, L. (2015). Mitochondrial CB1 receptor is involved in ACEA-induced protective effects on neurons and mitochondrial functions. Sci. Rep. *5*, 12440.

Marchi, S., Corricelli, M., Branchini, A., Vitto, V.A.M., Missiroli, S., Morciano, G., Perrone, M., Ferrarese, M., Giorgi, C., Pinotti, M., et al. (2019). Akt-mediated phosphorylation of MICU1 regulates mitochondrial Ca^{2+} levels and tumor growth. EMBO J. *38*, e99435.

Márkus, N.M., Hasel, P., Qiu, J., Bell, K.F., Heron, S., Kind, P.C., Dando, O., Simpson, T.I., and Hardingham, G.E. (2016). Expression of mRNA Encoding Mcu and Other Mitochondrial Calcium Regulatory Genes Depends on Cell Type, Neuronal Subtype, and Ca2+ Signaling. PLoS ONE *11*, e0148164.

Martín, R., Bajo-Grañeras, R., Moratalla, R., Perea, G., and Araque, A. (2015). Circuit-specific signaling in astrocyte-neuron networks in basal ganglia pathways. Science *349*, 730–734.

Martin-Fernandez, M., Jamison, S., Robin, L.M., Zhao, Z., Martin, E.D., Aguilar, J., Benneyworth, M.A., Marsicano, G., and Araque, A. (2017). Synapse-specific astrocyte gating of amygdala-related behavior. Nat Neurosci *20*, 1540–1548.

McClure, C., Cole, K.L., Wulff, P., Klugmann, M., and Murray, A.J. (2011). Production and titering of recombinant adeno-associated viral vectors. J. Vis. Exp. *57*, e3348.

Metna-Laurent, M., and Marsicano, G. (2015). Rising stars: modulation of brain functions by astroglial type-1 cannabinoid receptors. Glia *63*, 353–364.

Min, R., and Nevian, T. (2012). Astrocyte signaling controls spike timing-dependent depression at neocortical synapses. Nat *15*, 746–753.

National Research Council Committee (2011). Guide for the Care and Use of Laboratory Animals, Eighth Edition (National Academic Press).

Navarrete, M., and Araque, A. (2008). Endocannabinoids mediate neuron-astrocyte communication. Neuron *57*, 883–893.

Navarrete, M., and Araque, A. (2010). Endocannabinoids potentiate synaptic transmission through stimulation of astrocytes. Neuron *68*, 113–126.

Navarrete, M., Díez, A., and Araque, A. (2014). Astrocytes in endocannabinoid signalling. Philos Trans R Soc Lond B Biol Sci *369*, 20130599.

Nedergaard, M., Ransom, B., and Goldman, S.A. (2003). New roles for astrocytes: redefining the functional architecture of the brain. Trends Neurosci. *26*, 523–530.

O-Uchi, J., Pan, S., and Sheu, S.S. (2012). Perspectives on: SGP symposium on mitochondrial physiology and medicine: molecular identities of mitochondrial Ca2+ influx mechanism: updated passwords for accessing mitochondrial Ca2+-linked health and disease. J. Gen. Physiol. *139*, 435–443.

Ohkura, M., Sasaki, T., Sadakari, J., Gengyo-Ando, K., Kagawa-Nagamura, Y., Kobayashi, C., Ikegaya, Y., and Nakai, J. (2012). Genetically encoded green fluorescent Ca2+ indicators with improved detectability for neuronal Ca2+ signals. PLoS ONE *7*, e51286.

Ohno-Shosaku, T., Maejima, T., and Kano, M. (2001). Endogenous cannabinoids mediate retrograde signals from depolarized postsynaptic neurons to presynaptic terminals. Neuron *29*, 729–738.

Oliveira da Cruz, J.F., Robin, L.M., Drago, F., Marsicano, G., and Metna-Laurent, M. (2016). Astroglial type-1 cannabinoid receptor (CB1): A new player in the tripartite synapse. Neuroscience *323*, 35–42.

Ortinski, P.I., Dong, J., Mungenast, A., Yue, C., Takano, H., Watson, D.J., Haydon, P.G., and Coulter, D.A. (2010). Selective induction of astrocytic gliosis generates deficits in neuronal inhibition. Nat. Neurosci. *13*, 584–591.

Pagano Zottola, A.C., Soria-Gomez, E., Bonilla-del-Río, I., Muguruza, C., Terral, G., Robin, L.M., da Cruz, J.F.O., Redon, B., Lesté-Lasserre, T., Tolentino-Cortes, T., et al. (2020). A new mutant mouse model lacking mitochondrial-associated CB1 receptor. bioRxiv. https://doi.org/10.1101/2020.03.30.009472.

Perea, G., and Araque, A. (2005). Synaptic regulation of the astrocyte calcium signal. J. Neural Transm. (Vienna) *112*, 127–135.

Perea, G., Navarrete, M., and Araque, A. (2009). Tripartite synapses: astrocytes process and control synaptic information. Trends Neurosci. *32*, 421–431.

Pérez-Alvarez, A., and Araque, A. (2013). Astrocyte-neuron interaction at tripartite synapses. Curr. Drug Targets *14*, 1220–1224.

Perez-Alvarez, A., Navarrete, M., Covelo, A., Martin, E.D., and Araque, A. (2014). Structural and functional plasticity of astrocyte processes and dendritic spine interactions. J Neurosci *34*, 12738–12744.

Piomelli, D. (2003). The molecular logic of endocannabinoid signalling. Nat. Rev. Neurosci. *4*, 873–884.

Pnevmatikakis, E.A., and Giovannucci, A. (2017). NoRMCorre: An online algorithm for piecewise rigid motion correction of calcium imaging data. J. Neurosci. Methods *291*, 83–94.

Raastad, M. (1995). Extracellular activation of unitary excitatory synapses between hippocampal CA3 and CA1 pyramidal cells. Eur. J. Neurosci. *7*, 1882–1888.

Raffaello, A., De Stefani, D., Sabbadin, D., Teardo, E., Merli, G., Picard, A., Checchetto, V., Moro, S., Szabò, I., and Rizzuto, R. (2013). The mitochondrial calcium uniporter is a multimer that can include a dominant-negative pore-forming subunit. EMBO J. *32*, 2362–2376.

Rasooli-Nejad, S., Palygin, O., Lalo, U., and Pankratov, Y. (2014). Cannabinoid receptors contribute to astroglial Ca^{2+}-signalling and control of synaptic plasticity in the neocortex. Philos Trans R Soc Lond B Biol Sci *369*, 20140077.

Reyes, R.C., and Parpura, V. (2008). Mitochondria modulate Ca2+-dependent glutamate release from rat cortical astrocytes. J. Neurosci. *28*, 9682–9691.

Rizzuto, R., Nakase, H., Darras, B., Francke, U., Fabrizi, G.M., Mengel, T., Walsh, F., Kadenbach, B., DiMauro, S., and Schon, E.A. (1989). A gene specifying subunit VIII of human cytochrome *c* oxidase is localized to chromosome 11 and is expressed in both muscle and non-muscle tissues. J. Biol. Chem. *264*, 10595–10600.

Rizzuto, R., Brini, M., Murgia, M., and Pozzan, T. (1993). Microdomains with high Ca2+ close to IP3-sensitive channels that are sensed by neighboring mitochondria. Science *262*, 744–747.

Rizzuto, R., Brini, M., Pizzo, P., Murgia, M., and Pozzan, T. (1995). Chimeric green fluorescent protein as a tool for visualizing subcellular organelles in living cells. Curr. Biol. *5*, 635–642.

Rizzuto, R., De Stefani, D., Raffaello, A., and Mammucari, C. (2012). Mitochondria as sensors and regulators of calcium signalling. Nat. Rev. Mol. Cell Biol. *13*, 566–578.

Robin, L.M., Oliveira da Cruz, J.F., Langlais, V.C., Martin-Fernandez, M., Metna-Laurent, M., Busquets-Garcia, A., Bellocchio, L., Soria-Gomez, E., Papouin, T., Varilh, M., et al. (2018). Astroglial CB_1 Receptors Determine Synaptic D-Serine Availability to Enable Recognition Memory. Neuron *98*, 935–944.

Sakuragi, S., Niwa, F., Oda, Y., Mikoshiba, K., and Bannai, H. (2017). Astroglial Ca^{2+} signaling is generated by the coordination of IP_3R and store-operated Ca^{2+} channels. Biochem. Biophys. Res. Commun. *486*, 879–885.

Santo-Domingo, J., and Demaurex, N. (2010). Calcium uptake mechanisms of mitochondria. Biochim. Biophys. Acta *1797*, 907–912.

Scemes, E., and Giaume, C. (2006). Astrocyte calcium waves: what they are and what they do. Glia *54*, 716–725.

Schnütgen, F., Doerflinger, N., Calléja, C., Wendling, O., Chambon, P., and Ghyselinck, N.B. (2003). A directional strategy for monitoring Cre-mediated recombination at the cellular level in the mouse. Nat. Biotechnol. *21*, 562–565.

Semyanov, A. (2019). Spatiotemporal pattern of calcium activity in astrocytic network. Cell Calcium *78*, 15–25.

Sherwood, M.W., Arizono, M., Hisatsune, C., Bannai, H., Ebisui, E., Sherwood, J.L., Panatier, A., Oliet, S.H., and Mikoshiba, K. (2017). Astrocytic IP_3 Rs: Contribution to Ca^{2+} signalling and hippocampal LTP. Glia *65*, 502–513.

Simpson, P.B., Mehotra, S., Lange, G.D., and Russell, J.T. (1997). High density distribution of endoplasmic reticulum proteins and mitochondria at specialized Ca2+ release sites in oligodendrocyte processes. J. Biol. Chem. *272*, 22654–22661.

Soria-Gomez, E., Pagano Zottola, A.C., Mariani, Y., Desprez, T., Barresi, M., Bonilla-Del Río, I., Muguruza, C., Le Bon-Jego, M., Julio-Kalajzić, F., Flynn, R., et al. (2021). Subcellular specificity of cannabinoid effects in striatonigral circuits. Neuron *109*, 1513–1526.e11.

Stephen, T.L., Higgs, N.F., Sheehan, D.F., Al Awabdh, S., López-Doménech, G., Arancibia-Carcamo, I.L., and Kittler, J.T. (2015). Miro1 Regulates Activity-Driven Positioning of Mitochondria within Astrocytic Processes Apposed to Synapses to Regulate Intracellular Calcium Signaling. J. Neurosci. *35*, 15996–16011.

Suofu, Y., Li, W., Jean-Alphonse, F.G., Jia, J., Khattar, N.K., Li, J., Baranov, S.V., Leronni, D., Mihalik, A.C., He, Y., et al. (2017). Dual role of mitochondria in producing melatonin and driving GPCR signaling to block cytochrome *c* release. Proc. Natl. Acad. Sci. USA *114*, E7997–E8006.

Tarasova, N.V., Vishnyakova, P.A., Logashina, Y.A., and Elchaninov, A.V. (2019). Mitochondrial Calcium Uniporter Structure and Function in Different Types of Muscle Tissues in Health and Disease. Int. J. Mol. Sci. *20*, 4823.

Volterra, A., and Meldolesi, J. (2005). Astrocytes, from brain glue to communication elements: the revolution continues. Nat. Rev. Neurosci. *6*, 626–640.

Volterra, A., Liaudet, N., and Savtchouk, I. (2014). Astrocyte Ca^{2+} signalling: an unexpected complexity. Nat. Rev. Neurosci. *15*, 327–335.

Williams, G.S., Boyman, L., Chikando, A.C., Khairallah, R.J., and Lederer, W.J. (2013). Mitochondrial calcium uptake. Proc. Natl. Acad. Sci. USA *110*, 10479–10486.

Wilson, R.I., and Nicoll, R.A. (2001). Endogenous cannabinoids mediate retrograde signalling at hippocampal synapses. Nature *410*, 588–592.

Xu, Z., Lv, X.A., Dai, Q., Ge, Y.Q., and Xu, J. (2016). Acute upregulation of neuronal mitochondrial type-1 cannabinoid receptor and it's role in metabolic defects and neuronal apoptosis after TBI. Mol. Brain *9*, 75.

Zou, S., and Kumar, U. (2018). Cannabinoid Receptors and the Endocannabinoid System: Signaling and Function in the Central Nervous System. Int. J. Mol. Sci. *19*, 833.

CellPress
OPEN ACCESS

STAR★METHODS

KEY RESOURCES TABLE

REAGENT or RESOURCE	SOURCE	IDENTIFIER
Antibodies		
Rabbit anti-Tomm20	Santa Cruz Biotechnologies	Cat # sc-11415 RRID:AB_2207533
Rabbit p-Akt (Ser473)	Cell Signaling Technology	Cat # 9271 RRID:AB_329825
Mouse anti-myc	Roche	Cat # 11667149001 RRID:AB_390912
Guinea pig anti-CB_1	Abyntek	Cat # CB_1-gp-AF530 RRID:AB_2314113
Mouse anti-NeuN	Millipore	Cat # MAB377 RRID:AB_2298772
Rabbit anti-GFP	Invitrogen	Cat # A11122 RRID:AB_221569
Mouse anti-S100β	Sigma Aldrich	Cat # AMAB91038 AB_2665776
Rabbit anti-GFAP	DAKO	Cat # Z0334 RRID:AB_10013382
Bacterial and virus strains		
AAV-hGFAP-Cre-IRES-mCherry	University of North Caroline	N/A
AAV-GFAP-Mito-GCaMP6s	This paper	N/A
AAV-GFAP-dnMCU-IRES-mRuby	This paper	N/A
AAV-Flex-CB_1-myc	This paper	N/A
AAV-Flex-DN22-CB_1-myc	This paper	N/A
Chemicals, peptides, and recombinant proteins		
THC	THC Pharm GmbH	Cat # THC-1098E
WIN55-212-2	Sigma-Aldrich	Cat # W102
2-APB	Tocris	Cat # 1224
Thapsigargin	Sigma-Aldrich	Cat # T9033
ATP	Sigma-Aldrich	Cat # A26209
MCU-i11	ChemDiv	Cat # C728-0199
MK-2206	Enzo Life Sciences	Cat # ENZ-CHM164
Experimental models: Organisms/strains		
CB_1 KO	The Jackson Laboratory	Cat # 036108
DN22-CB_1-KI	(Soria-Gomez et al., 2021)	N/A
Recombinant DNA		
Mito-GCaMP6s	This paper	N/A
RCaMP2	(Inoue et al., 2015)	N/A
MCU-D260N-E263Q	(Raffaello et al., 2013)	N/A
MICU1-WT	(Marchi et al., 2019)	N/A
MICU1-S124A	(Marchi et al., 2019)	N/A
DN22-CB_1	(Hebert-Chatelain et al., 2016)	N/A
Software and algorithms		
Prism 9	GraphPad	https://www.graphpad.com/scientific-software/prism/: RRID:SCR_002798
FIJI	ImageJ	https://imagej.net/software/fiji/ RRID:SCR_002285
MATLAB R2018a	MATLAB	http://www.mathworks.com/products/matlab/: RRID:SCR_001622
Calcium event analysis code	This paper	https://doi.org/10.5281/zenodo.5682226

RESOURCE AVAILABILITY

Lead contact

Further information and requests for resources and reagents should be directed to and will be fulfilled by the lead contact, Giovanni Marsicano (giovanni.marsicano@inserm.fr).

Materials availability

This study did not generate new unique reagents.

Data and code availability

All data reported in this paper will be shared by the lead contact upon request. Original code for calcium event analysis has been deposited on "Zenodo:https://doi.org/10.5281/zenodo.568226)" and is publicly available as of the date of publication. Any additional information required to reanalyze the data reported in this paper is available from the lead contact upon request.

EXPERIMENTAL MODEL AND SUBJECT DETAILS

Mice

All experiments were performed in accordance with the Guide for the Care and Use of Laboratory Animals (National Research Council Committee, 2011) and the European Communities Council Directive of September 22th 2010 (2010/63/EU, 74). Experiments were approved by the local ethical committee of the University of Bordeaux (approval number 501350-A) and the French Ministry of Agriculture and Forestry (authorization number 3306369). *CB$_1$* WT and *CB$_1$* KO male littermate mice (8-16 weeks of age) were used for two-photon experiments and fiber photometry experiments. Cages were enriched and mice were maintained under standard conditions (food and water *ad libitum*; 12 h–12 h light–dark cycle. Fiber photometry experiments were done during dark cycle (light off at 8:00a.m.). The rest of the experiments were performed between 9:00 and 19:00 (light on at 7:00). Pups (P0-P1) for primary cell cultures were obtained from homozygote *CB$_1$* KO pairs. Slices for electrophysiology were obtained from *CB$_1$*-flox mice (8-16 weeks of age). No method of randomization to assign experimental groups was performed and the number of mice in each experimental group was similar. No statistical methods were used to predetermine sample size.

Adeno-associated viruses (AAV)

AAV-hGFAP-Cre-IRES-mCherry was purchased from University of North Caroline (UNC School of Medicine). AAV-GFAP-Mito-GCaMP6s, AAV-GFAP-dnMCU-IRES-mRuby, AAV-Flex-CB$_1$-myc and AAV-Flex-DN22-CB$_1$-myc viral constructs were subcloned using standard molecular cloning techniques previously used in the lab (Hebert-Chatelain et al., 2016). The resulting vector was transfected with PEI into HEK293 cells together with the AAV8-serotype-packaging plasmids (Hammond et al., 2017), the viruses were then purified by Iodixanol desnity gradient and titerd as previously described (McClure et al., 2011). Virus titers were between 10^{10} and 10^{11} genomic copies per ml for all batches of virus used in the study.

Cell culture and transfection

Primary cortical astroglial cultures were prepared from *CB$_1$* KO P0–P1 mice. Briefly, brains were extracted in PBS containing 0.6% glucose and 0.5% bovine serum albumin (BSA), the cortex were dissected. To dissociate cells 0.25% trypsin (Invitrogen, France) and DNase (Roche, Basel, Switzerland) were used in HBSS 1x. Cells were seeded into 75 cm2 flask and after 2 weeks transferred to glass coverslips for live imaging and immunocytochemistry analysis. Astrocytes were kept in MEM (GIBCO, France) supplemented with 10% fetal bovine serum (FBS), 2 mM l-glutamine, 120 μg*ml−1 penicillin, 200 μg*ml−1 streptomycin, 1 mM pyruvate, 0.6% Glucose, Fungiozione (Invitrogen, France), and were maintained at 37°C in the presence of 5% CO2. Transfection was carried out at 1-2 days after coverslip seeding using a standard calcium phosphate transfection protocol, with a 1:1:4 DNA ratio of plasmids (RCaMP2: Mito-GCaMP6s: and empty vector, CB$_1$ or DN22-CB$_1$, respectively). For the experiments using the dnMCU or MICU1 under CMV promoter, this was used substituting RCaMP2. Astrocytes were cultured for 2 days after transfection before the recordings. Parallel immunocytochemistry showed a high degree of co-transfection of the cells expressing Mito-GCaMP6s and RCaMP2 with the non-tagged CB$_1$ vector (not shown). For anatomical studies myc tagged versions of CB$_1$ and DN22-CB$_1$ were used. For electron microscopy experiments, cells were infected at day 0 using AAV vectors encoding for CB$_1$, DN22-CB$_1$ or empty vector. 7 days after the infection were fixed as described below.

METHOD DETAILS

Drugs

THC was obtained from THC Pharm GmbH (Frankfurt, Germany). WIN55-212-2 (WIN), thapsigargin and ATP disodium salt-hydrate (ATP) were purchased from Sigma-Aldrich (St-Louis, USA); 2APB from Tocris (Bristol, UK); MCU-i11 from ChemDiv (San Diego, USA) and MK-2206 from Enzo Life Sciences (Farmingdale, USA). For *in vitro* experiments, WIN, 2APB, thapsigargin, MCU-i11 (Di Marco et al., 2020) and MK-2206 were dissolved in DMSO; ATP was dissolved in water. DMSO was never higher than 0.001%. For *in vivo*

administration, THC was prepared freshly before the experiments and was dissolved in a mixture of 5% ethanol, 4% cremophor and saline. MK was prepared freshly before experiments and was dissolved in a mixture of 7% DMSO, 1.25% Tween-80 and saline. Corresponding vehicle solutions were used in control experiments. Doses and concentrations of the different drugs were chosen based on previous published data or preliminary experiments.

Plasmids

The plasmid coding for Mito-GCaMP6s was obtained using standard cloning techniques. Briefly, GcaMP6s (Addgene) starting codon was mutated and the resulting sequence was subcloned into a plasmid containing the mitochondria targeting sequence (MTS) derived from the subunit VIII of human cytochrome C oxidase (Rizzuto et al., 1989, 1995). RCaMP2 was a generous gift from Prof. H. Bito (Inoue et al., 2015). The N-terminal deletion of the first 22 aminoacids in the mouse CB_1 receptor coding sequence to obtain DN22-CB_1 mutant was achieved as previously described in Hebert-Chatelain et al. (2016). The plasmid encoding for the dominant negative version of MCU in pcDNA3.1 plasmid (MCU-D260N-E263Q, dnMCU (Raffaello et al., 2013)) was a generous gift from Dr. D. De Stefani (University of Padova, Italy). The plasmids encoding for MICU1-WT and MICU1-S124A (Marchi et al., 2019) was a generous gift from Prof. Paolo Pinton (University of Ferrara, Italy).

Immunocytochemistry

Astrocytes were fixed in 4% formaldehyde dissolved in PBS (0.1 M, pH 7.4). Cells were pre-incubated in a blocking solution (10% normal goat serum, 0.1% Triton X-100 and 0.2 M glycine in PBS) for 1 h and then incubated with primary antibody in the same blocking solution for 2 h. Primary antibodies were rabbit anti-TOM20 (1:500; Santa Cruz, sc-11415), mouse anti-myc (1:500; Roche, 11667149001), rabbit p-Akt (Ser473) (1:100; Cell Signaling Technology, 9271) or guinea pig anti-CB_1 (1:300; Abyntek, CB_1-gp-AF530). Secondary fluorescent antibodies anti-mouse Alexa488 or anti-rabbit Alexa647 (1:800; Invitrogen) or Atto 647N (Sigma Aldrich) for STED experiments were incubated in blocking solution for 1 h. Then, cells were washed and mounted with fluoromont-G (Electron Microscopy Sciences). All the procedures were carried out at room temperature. For p-AKt experiments astrocytes were imaged with a Confocal Leica DMI6000 microscope (Leica) and the image analysis was done with ImageJ software (NIH, USA).

STED imaging and quantification

Astrocytes were processed for immunocytochemistry as described above and imaged using a LEICA SP8 WLL2 on an inverted stand DMI6000 (Leica Microsystems, Mannheim, Germany) and objective HC PL APO 100X oil STED NA 1.40. The depletion lasers used were 660 nm and 775 nm. For overlap analysis, average+5*std from the entire control images was considered as background and the correspondent threshold applied to all images. Then the overlap area over total mitochondria area (Tom20) was calculated. For distance map analysis a threshold equivalent to average+3*std of the control condition was applied to all images and "Distance Map" function from ImageJ software (NIH, USA) used. The resulting images and the data obtained grouped every 0,126 μm (6*pixel size). All image analysis was done with ImageJ software (NIH, USA).

Electron microscopy

Astrocytes were fixed for 45 min at 4 °C in 4% glutaraldehyde in PBS, washed and fixed again 1 h at room temperature in 2% osmium tetroxide in PBS containing 15 mg/ml of $K_4Fe(CN)_6$. Dehydration was performed with ethanol series (50%, 70%, 95% and absolute ethanol). Thereafter, the samples were embedded progressively in Epon resin. Ultrathin sections were contrasted with 1% lead citrate in water for 1 min. Sample imaging was performed using a Hitachi H7650 transmission microscope operated at 80 KV with a camera Gatan—11 MPx at electron microscopy unit (Bordeaux imaging center). For data analysis, mitochondria and ER were manually selected and interfaces between ER and mitochondria were measured using the ImageJ plugin MitoCare (Bartok et al., 2019). The threshold to identify a contact between ER and mitochondria is a "Ca_score" higher than 5.

Live cell imaging and data analysis

Calcium imaging (Mito-GCaMP6s and RCaMP2) in cortical astrocytes was recorded using an inverted Leica DMI6000 microscope (Leica Microsystems, Wetzlar, Germany) equipped with a confocal Scanner Unit CSU-X1 (Yokogawa Electric Corporation, Tokyo, Japan) and a Evolve EMCCD camera (Photometrics, Tucson, USA). The diode lasers used were at 491 nm and 561 nm and the objective was a HCX PL Apo CS 63 × oil 1.4 NA. The 37°C atmosphere during time-lapse image acquisition was created with an incubator box and an air heating system (Life Imaging Services, Basel, Switzerland). This system was controlled by MetaMorph software (Molecular Devices, Sunnyvale, USA). Only one focal plane was manually selected and recorded every 5 s using an auto-focus system to avoid movement artifacts. Culture media supplemented with 25 μM HEPES was perfused continuously and the different compounds added to the media when desired. On the basis of preliminary experiments WIN was added 15 min after the starting of the recording and ATP 20 min after WIN.

Image processing, analysis, and editing were done with ImageJ software (NIH, USA). RCaMP2 measurement linearly adjusted to correct the bleaching of the sample. The signal was averaged every 30 s and the corrected calcium signal (ΔF/F0) was calculated. For

both, mitochondrial and cytosolic calcium signals, F0 corresponds to 1 min average before the WIN or ATP application and the area under the curve (AUC) was quantified 4 min after. ATP null responses (except during the irreversible thapsigargin treatment) were considered criteria of exclusion.

Fluorescence immunohistochemistry

Mice were anaesthetized with chloral hydrate (400 mg*kg−1 body weight) and transcardially perfused with phosphate-buffered solution (PB 0.1 M, pH 7.4) followed by 4% formaldehyde dissolved in PBS (0.1 M, pH 7.4). After perfusion, the brains were removed and incubated several additional hours in the same fixative and finally the brain were embedded with sucrose 30% for 3 days, frozen, and kept at −80°C degrees. Serial brain coronal cryosections were cut at 40 μm and collected in 0.1 M PB (pH 7.4) at room temperature (RT.)

Immunofluorescence NeuN/GFP Sections were pre-incubated in a blocking solution of 10% donkey serum, 0.02% sodium azide and 0.3% Triton X-100 prepared in PBS for 30 min–1 h at room temperature. Free-floating sections were incubated overnight (4°C) with mouse anti-NeuN (1:500; Millipore, MAB377), rabbit anti-GFP (1:1000; Invitrogen, A11122). The antibodies were prepared in 10% donkey serum in PBS containing 0.02% sodium azide and 0.3% Triton X-100. Then, the sections were washed in PBS for 30 min at room temperature. The tissue was incubated with fluorescent anti-rabbit Alexa488, anti-mouse Alexa546 (1:500, Invitrogen) for 2 h and washed in PBS at room temperature. Finally, sections were washed, mounted, dried, and a coverslip was added on top with DPX (Fluka Chemie AG). The slides were analyzed with Confocal Leica DMI6000 microscope or epifluorescence Leica DM6000 microscope (Leica).

Immunofluorescence S100β/GFP Sections were blocked with 3% H_2O_2 during 30 min. Free-floating sections were incubated overnight (4°C) with rabbit anti-GFP (1:1000; Invitrogen, A11122), mouse anti-S100β (1:500; Sigma Aldrich, AMAB91038). The antibodies were prepared in 10% donkey serum in PBS containing 0.02% sodium azide and 0.3% Triton X-100. Then, the sections were washed in PBS for 30 min at room temperature. The tissue was incubated with fluorescent anti-mouse HRP (1:500, Cell Signaling) and anti-rabbit Alexa488 (1:500, Invitrogen) for 2 h and washed in PBS at room temperature. After, section were incubated with TSA Cy3 (1:300, 10 min, Perkin Elmer). Finally, sections were washed, mounted, dried, and a coverslip was added on top with DPX (Fluka Chemie AG). The slides were analyzed with Confocal Leica DMI6000 microscope or epifluorescence Leica DM6000 microscope (Leica).

Immunofluorescence GFAP Sections were pre-incubated in a blocking solution of 10% donkey serum, 0.02% sodium azide and 0.3% Triton X-100 prepared in PBS for 30 min–1 h at room temperature. Free-floating sections were incubated overnight (4°C) with rabbit anti-GFAP (1:500; DAKO, Z0334). The antibody was prepared in 10% donkey serum in PBS containing 0.02% sodium azide and 0.3% Triton X-100. Then, the sections were washed in PBS for 30 min at room temperature. The tissue was incubated with fluorescent anti-rabbit Alexa 647 (1:500, Invitrogen) for 2 h and washed in PBS at room temperature. Finally, sections were washed, mounted, dried, and a coverslip was added on top with DPX (Fluka Chemie AG). The slides were analyzed with Confocal Leica DMI6000 microscope or epifluorescence Leica DM6000 microscope (Leica).

Surgery and AAV administration

Mice (7–10 weeks of age) were anaesthetized by isoflurane or, for two-photon experiments, by an intraperitoneal (i.p.) injection of a mix containing medetomidine (sededorm, 0.27 mg/kg) and midazolam (Dormicum, 5 mg/kg) in sterile NaCl 0.9% (MMF-mix). Analgesia was achieved by local application of 100 μl of lidocaine (lurocaine, 1%) and subcutaneous (s.c.) injection of buprenorphine (buprécare, 0.05 mg/kg). For two-photon experiments, mice were additionally administrated 40 μl of dexamethasone (dexadreson, 0.1 mg/ml) intramuscularly (i.m.) in the quadriceps to reduce the cortical stress during the surgery and to prevent inflammation potentially caused by the friction of the drilling. A heating-pad was positioned underneath the animal to keep the body temperature at 37°C. Eye dehydration was prevented by topical application of ophthalmic gel. The skin above the skull was shaved with a razor and disinfected with modified ethanol 70% and betadine before an incision was made. Mice were placed into a stereotaxic apparatus (David Kopf Instruments) with mouse adaptor and lateral ear bars.

Cranial window implantation and AAV delivery for two-photon experiments were made as previously described (Gambino et al., 2014; Holtmaat et al., 2009). Briefly, the bregma and lambda were aligned (x and z) after skull's exposure a ∼5 mm custom plastic chamber was attached on the area of interest and a 3 mm craniotomy was made on the right hemisphere above the primary somatosensory cortex, with a pneumatic dental drill (BienAir Medical Technologies, AP-S001), leaving the dura intact. The stereotaxic injections were targeted to the layer 2/3 of the barrel cortex (from bregma: anterior–posterior – 1.5; medial–lateral ± 2.5). 200 nL of virus AAV-GFAP-Mito-GCaMP6s were injected at a maximum rate of 60 nl/min, using a glass pipette (Wiretrol, Drummond) attached to an oil hydraulic manipulator (MO-10, Narishige). After injections, the virus was allowed to diffuse for at least 30 min before the pipette was withdrawn. The craniotomy was covered with sterile saline (0.9% NaCl) and sealed with a 3 mm glass coverslip after viral injection. The chamber, the coverslip and a custom-made stainless steel head stage were well attached to the skull using dental acrylic and dental cement (Jet Repair Acrylic, Lang Dental Manufacturing). Mice were then waked-up by a sub-cutaneous injection of a mixture containing atipamezole (revertor, 2.5 mg/kg), flumazenil (0.5 mg/kg), and buprenorphine (buprécare, 0.1 mg/kg) in sterile NaCl 0.9%. For other viral intrahippocampal and intracortical AAV delivery, AAV vectors were injected with the help of a glass pipette attached to a Nanoject III (Drummond, Broomall, USA). Mice were injected 0.4 μL per injection site at a rate of 0.3 μL per min with the following coordinates: posterior hippocampus, anterior–posterior – 2.6; medial–lateral ± 2.15; dorsal–ventral − 2.0 and − 1.5 (for

electrophysiology recordings); anterior hippocampus (anterior–posterior – 2; medial–lateral ± 1; dorsal–ventral – 2.0 (for fiber photometry experiments) and motor cortex: anterior–posterior – 1; medial–lateral ± 1; dorsal–ventral – 0.5 (for fiber photometry). Following virus delivery, the syringe was left in place for 3 min before being slowly withdrawn from the brain. For fiber photometry experiments, the optical fiber (400 μm diameter) was placed 250 μm above the injection site. Mito-GCaMP6s or dnMCU expression was verified by fluorescent immunohistochemistry (see above). Animals were used for experiments 2-4 weeks after injections before experiments.

2-photon laser-scanning microscope (2PSLM)

2 weeks after the surgery, anesthetized mice (isoflurane 2%, body temperature maintained at 37°C, and eyes protected from dehydration) were imaged longitudinally using an *in vivo* non-descanned FemtoSmart 2PLSM (Femtonics, Budapest, Hungary) equipped with resonant scanners (operating at 37 Hz) and a × 16 objective (0.8 NA, Nikon). The MES Software (MES v.4.6; Femtonics, Budapest, Hungary) was used to control the microscope, the acquisition parameters, and the TTL-driven synchronization. Mito-GcaMP6s was excited using a Ti:sapphire laser operating at $\lambda = 910$ nm (Mai Tai DeepSee, Spectra-Physics) with an average excitation power at the focal point lower than 50 mW. Fluorescence from mitochondria expressing GcaMP6s was collected from the same field of view (400 × 400 μm) for 3 consecutive days (one condition per day) for 45 min without injection (day 1), before and after the injection of vehicle (day 2), and before/after the injection of THC (day 3). Manual intraperitoneal injection of either vehicle or THC solution were performed under infrared camera control (Imetronic) during imaging using a custom made tubing system and a needle inserted in the animal prior to recording.

Images from an individual 45 min acquisition session were first laterally realigned so as to compensate for slow, micrometric drift of the field of view. At full temporal resolution (37 Hz), we first used a method for correcting lateral translation with sub-pixel accuracy (Pnevmatikakis and Giovannucci, 2017) which works by matching individual images to a dynamically changing template image. We then binned data to 1 Hz to enhance signal-to-noise ratio and re-run the alignment procedure to improve on long-term stability. For each pixel, a time-series of fluorescence fluctuations ($\Delta F/F_0$) was then computed. For each time point t, F was computed as the median fluorescence signal from t to t+30 s, F_0 was the median fluorescence from t-30 s to t, and $\Delta F/F_0 = (F - F_0)/F_0$. Large increase of pixel-wise fluorescence was initially detected based on the criteria $\Delta F/F_0 > 5\%$. In order to discard spurious increase events that could not be accounted by mitochondrial events (eg noise), we performed morphological opening with a disk of 1-pixel radius of the binary event images (in effect removing isolated pixels too small to be mitochondria). We then grouped clustered positive pixels in the 2D+T stack of images by connected component analysis in 3D (18-connected neighborhood) in order to obtain the final list of temporally and spatially localized mitochondrial fluorescence events. Datasets from different imaging sessions were temporally realigned by using the time of i.p. injection as a reference point. For Figure 3F, in each session, we counted the number of fluorescence increase events per 5 min temporal bin and normalized these counts by that of events during the 10 min period immediately preceding injection (Baseline) so as to compensate for injection-independent inter-session and inter-animal variability.

Fiber photometry imaging

3-4 weeks after the surgery Freely-moving mice imaged using 470 and 405 nm LEDs to excite Mito-GCaMP6s 3-4 weeks after surgery, after 1 day of handling habituation. The emitted fluorescence is proportional to the calcium concentration for stimulation at 470 nm (Akerboom et al., 2013; Ohkura et al., 2012). The isosbestic stimulation (UV light, 405 nm) was also used in alternation with the blue light (470 nm) to treat the signal after, as the fluorescence emitted after this stimulation is not depending on calcium (Lütcke et al., 2010). The GCaMP6s fluorescence from the astrocytes was collected with a sCMOS camera through an optic fiber divided in 2 sections: a short fiber implanted in the brain of the mouse and a long fiber (modified patchcord), both connected through a ferrule-ferrule (1.25 mm) connection. MATLAB program (Matlabworks) was used to synchronize each image recording made by the camera, and the Mito-GCaMP6s light excitation made by the LEDs (470 and 405 nm). The two wavelengths of 470 and 405 nm at a power of 0.1 mW were alternated at a frequency of 20 Hz each (40 Hz alternated light stimulations).

To extract the fluorescence signal specific to calcium fluctuation, and to remove bleaching and movement artifacts, a subtraction of the isosbestic 405 nm signal to the calcium signal (470 nm) was performed. A sliding window average of 2 min was used and ratiometric calcium signal calculated ($\Delta F/F_0$). Then calcium transients were detected on the filtered trace (high filter) using a threshold to identify them (2*median absolute deviation [MAD] of the baseline before injection, Figure 3J). The first minute previous and after injection were removed from quantification to exclude injection effects and transients were divided in two equal periods of near 15 min each. All data processing was performed using custom MATLAB scripts.

Hippocampal slice preparation

Animals were decapitated and the brain was rapidly removed and placed in ice-cold cutting solution that contained (in mM): sucrose 180, KCl 2.5, NaH_2PO_4 1.25, $NaHCO_3$ 26, $MgCl_2$ 12, $CaCl_2$ 0.2, glucose 11, and was gassed with 95% O_2/5% CO_2 (pH = 7.3–7.4). 350-μm thick coronal slices were cut with a vibratome (VT1200S, Leica) and incubated in ACSF at 34°C. After 30 min slices were kept at room temperature. ACSF contained (in mM): NaCl 123, KCl 2.5, NaH_2PO_4 1.25, $NaHCO_3$ 26, $MgCl_2$ 1.3, $CaCl_2$ 2.5, and glucose 11, and was gassed with 95% O_2/5% CO_2 (pH = 7.3–7.4). Slices were transferred to an immersion recording chamber, superfused at 2 ml/min with gassed ACSF and visualized under an Olympus microscope (Olympus Optical).

Electrophysiology

Electrophysiological simultaneous recordings from 2 CA1 pyramidal neurons (> 60 μm apart) were made in whole-cell configuration of the patch-clamp technique. Patch electrodes had resistances of 3–8 MΩ when filled with the internal solution containing (in mM): KCl 130, HEPES 10, EGTA 1, MgCl2 2, CaCl2 0.3, Phosphocreatine 7, Mg-ATP 3, Na-GTP 0.3 (pH = 7.3, 290 mOsm). Recordings were obtained with a MultiClamp 700B amplifier (Molecular devices). Membrane potential was held at −70 mV and series and input resistances were monitored throughout the experiment using a −5 mV pulse. Cells were discarded when series and input resistances changed > 20%. Signals were fed to a PC through a DigiData 1440A interface board. Signals were filtered at 1 KHz and acquired at 10 KHz sampling rate. The pCLAMP 10.7 (Axon instruments) software was used for stimulus generation, data display, acquisition, and storage. Excitatory postsynaptic currents (EPSCs) were isolated in the presence of picrotoxin (50 μM) and CGP54626 (1 μM) to block GABAA and GABAB receptors, respectively. All recordings were performed at 34°C.

Synaptic stimulation

Theta capillaries filled with ACSF were placed in the Stratum Radiatum for bipolar stimulation of Schaffer collaterals. Paired pulses (2 ms duration with 50 ms interval) were continuously delivered at 0.33 Hz using a Digitimer Ltd stimulator. Stimulus intensity (0.1–10 mA) was adjusted to meet the conditions that putatively stimulate single or very few presynaptic fibers (Allen and Stevens, 1994; Isaac et al., 1996; Raastad, 1995). Synaptic parameters analyzed were: success rate (ratio between the number of successes versus total number of stimuli) and EPSC amplitude (mean peak amplitude of the successes, excluding failures). A response was considered a failure if the amplitude of the current was < 3 times the standard deviation of the baseline current and was verified by visual inspection.

During the neuronal depolarization (ND) protocol one pyramidal neuron was depolarized to 0 mV for 5 s to stimulate endocannabinoid release (Chevaleyre and Castillo, 2004; Kreitzer and Regehr, 2001; Navarrete and Araque, 2008, 2010; Ohno-Shosaku et al., 2001; Wilson and Nicoll, 2001). To illustrate the time course of the effects of ND, synaptic parameters were grouped in 60 s bins. To determine synaptic changes, mean EPSCs (n = 60 EPSCs) recorded 3 min before the stimulus (basal) were compared with mean EPSCs (n = 20 EPSCs) recorded 1 min after ND. The presence of synaptic potentiation was determined to occur when the success rate increased more than two standard deviations from the baseline.

Confocal acquisition of calcium events

Neuronal depolarization (to 0 mV, 5 s) was made using a Patchmaster software and an EPC10 amplifier (HEKA Elektronik, Lambrecht/Pfalz, Germany). Confocal acquisitions were performed using a Leica SP5 on an upright stand DM6000 (Leica Microsystems, Mannheim, Germany) and with a 20 × (NA 1) water immersion objective. Images were acquired every 0.55-0.66 s using a 488 nm Argon laser and a 543 nm Helium/Neon laser for GCaMP6f and SR101 respectively. Pixel size was 0.55 μm.

Image analysis was done using a custom ImageJ macro (available on Zenodo: https://doi.org/10.5281/zenodo.5682226). Briefly, images were first laterally realigned so as to compensate for slow, micrometric drift of the field of view. Then, calcium events (above mean+4*std) were isolated and selected in 3 dimensions (x, y, t) using 3D object counter and 3D viewer ImageJ plugins. Size exclusion thereshold was set at 40 pixels. From each calcium event, the amplitude, frequency, duration, and spreading coefficient (max x distance * max y distance) were calculated. For quantification purposes only the mean values (per slice) of the calcium events starting 30 s before or 30 s after neuronal depolarization were considered.

QUANTIFICATION AND STATISTICAL ANALYSIS

Statistical analyses

All graphs and statistical analyses were performed using GraphPad software (version 5.0 or 6.0). Results were expressed as means of independent data points ± s.e.m. Parametric (or non-parametric when required) tests were used for the data and analyzed using the appropriate statistical test (detailed statistical data for each experiment are reported in Tables S1 and S2).